



2014-12

Environmental data collection using autonomous Wave Gliders

Hermsdorfer, Kathryn M.

Monterey, California: Naval Postgraduate School

<http://hdl.handle.net/10945/44577>



Calhoun is a project of the Dudley Knox Library at NPS, furthering the precepts and goals of open government and government transparency. All information contained herein has been approved for release by the NPS Public Affairs Officer.

Dudley Knox Library / Naval Postgraduate School
411 Dyer Road / 1 University Circle
Monterey, California USA 93943

<http://www.nps.edu/library>



**NAVAL
POSTGRADUATE
SCHOOL**

MONTEREY, CALIFORNIA

THESIS

**ENVIRONMENTAL DATA COLLECTION USING
AUTONOMOUS WAVE GLIDERS**

by

Kathryn M. Hermsdorfer

December 2014

Thesis Advisor:
Second Reader:

Qing Wang
Wendell Nuss

Approved for public release; distribution is unlimited

THIS PAGE INTENTIONALLY LEFT BLANK

REPORT DOCUMENTATION PAGE			<i>Form Approved OMB No. 0704-0188</i>	
Public reporting burden for this collection of information is estimated to average 1 hour per response, including the time for reviewing instruction, searching existing data sources, gathering and maintaining the data needed, and completing and reviewing the collection of information. Send comments regarding this burden estimate or any other aspect of this collection of information, including suggestions for reducing this burden, to Washington headquarters Services, Directorate for Information Operations and Reports, 1215 Jefferson Davis Highway, Suite 1204, Arlington, VA 22202-4302, and to the Office of Management and Budget, Paperwork Reduction Project (0704-0188) Washington, DC 20503.				
1. AGENCY USE ONLY (Leave blank)		2. REPORT DATE December 2014	3. REPORT TYPE AND DATES COVERED Master's Thesis	
4. TITLE AND SUBTITLE ENVIRONMENTAL DATA COLLECTION USING AUTONOMOUS WAVE GLIDERS			5. FUNDING NUMBERS	
6. AUTHOR(S) Kathryn M. Hermsdorfer				
7. PERFORMING ORGANIZATION NAME(S) AND ADDRESS(ES) Naval Postgraduate School Monterey, CA 93943-5000			8. PERFORMING ORGANIZATION REPORT NUMBER	
9. SPONSORING /MONITORING AGENCY NAME(S) AND ADDRESS(ES) N/A			10. SPONSORING/MONITORING AGENCY REPORT NUMBER	
11. SUPPLEMENTARY NOTES The views expressed in this thesis are those of the author and do not reflect the official policy or position of the Department of Defense or the U.S. Government. IRB Protocol number ___N/A___.				
12a. DISTRIBUTION / AVAILABILITY STATEMENT Approved for public release; distribution is unlimited			12b. DISTRIBUTION CODE A	
13. ABSTRACT (maximum 200 words) The Sensor Hosting Autonomous Remote Craft (SHARC), also known as Wave Glider, is an autonomous ocean vehicle powered by wave motion. This slow-moving platform makes long-term deployments and environmental data collection feasible, especially in data sparse regions or hazardous environments. The standard SHARC hosts a meteorological station (Airmar PB200) that samples air pressure, temperature, wind speed and wind direction at 1.12 m. The SHARC automatically transmits a 10-minute averaged data suite through an Iridium satellite link. In an effort to evaluate the SHARC default Airmar sensors and seek optimal sensors for air-sea interaction studies, NPS has developed an independent package of meteorological sensors, the "NPS Met," for use on the SHARC. NPS Met measures pressure, air temperature, wind, SST, and relative humidity. This SHARC payload package was deployed three times in the Monterey Bay, along with a collocated drifting buoy (Marine Air-Sea Flux buoy, or MASFlux) with proven flux, mean, wave, and SST measurement for comparison and validation. This thesis will present analyses of data from the new mast and Airmar as compared to known, quality measurements from NPS MASFlux and NDBC buoy. Surface fluxes, evaporation duct heights and strength are derived from the SHARC measurements using the COARE algorithm.				
14. SUBJECT TERMS SHARC, wave glider, Airmar, NPS Met, flux, mean measurements, air-sea interaction, surface layer			15. NUMBER OF PAGES 105	
			16. PRICE CODE	
17. SECURITY CLASSIFICATION OF REPORT Unclassified	18. SECURITY CLASSIFICATION OF THIS PAGE Unclassified	19. SECURITY CLASSIFICATION OF ABSTRACT Unclassified	20. LIMITATION OF ABSTRACT UU	

THIS PAGE INTENTIONALLY LEFT BLANK

Approved for public release; distribution is unlimited

**ENVIRONMENTAL DATA COLLECTION USING AUTONOMOUS WAVE
GLIDERS**

Kathryn M. Hermsdorfer
Lieutenant Commander, United States Navy
B.S., United States Naval Academy, 2000
M.S., University of Arkansas, 2010

Submitted in partial fulfillment of the
requirements for the degree of

**MASTER OF SCIENCE IN METEOROLOGY AND PHYSICAL
OCEANOGRAPHY**

from the

**NAVAL POSTGRADUATE SCHOOL
December 2014**

Author: Kathryn M. Hermsdorfer

Approved by: Qing Wang
Thesis Advisor

Wendell Nuss
Second Reader

Wendell Nuss
Chair, Department of Meteorology

THIS PAGE INTENTIONALLY LEFT BLANK

ABSTRACT

The Sensor Hosting Autonomous Remote Craft (SHARC), also known as Wave Glider, is an autonomous ocean vehicle powered by wave motion. This slow-moving platform makes long-term deployments and environmental data collection feasible, especially in data sparse regions or hazardous environments. The standard SHARC hosts a meteorological station (Airmar PB200) that samples air pressure, temperature, wind speed and wind direction at 1.12 m. The SHARC automatically transmits a 10-minute averaged data suite through an Iridium satellite link. In an effort to evaluate the SHARC default Airmar sensors and seek optimal sensors for air-sea interaction studies, NPS has developed an independent package of meteorological sensors, the “NPS Met,” for use on the SHARC. NPS Met measures pressure, air temperature, wind, SST, and relative humidity. This SHARC payload package was deployed three times in the Monterey Bay, along with a collocated drifting buoy (Marine Air-Sea Flux buoy, or MASFlux) with proven flux, mean, wave, and SST measurement for comparison and validation. This thesis will present analyses of data from the new mast and Airmar as compared to known, quality measurements from NPS MASFlux and NDBC buoy. Surface fluxes, evaporation duct heights and strength are derived from the SHARC measurements using the COARE algorithm.

THIS PAGE INTENTIONALLY LEFT BLANK

TABLE OF CONTENTS

I.	INTRODUCTION.....	1
A.	IMPORTANCE OF NEAR SURFACE	1
B.	RESEARCH OBJECTIVES	2
C.	NAVAL APPLICATIONS	3
1.	Electromagnetic Propagation	4
II.	BACKGROUND	5
A.	PHYSICAL PROCESSES AT THE AIR-SEA INTERFACE	5
B.	SURFACE FLUX.....	6
C.	MONIN-OBUKHOV SIMILARITY THEORY (MOST).....	8
D.	SURFACE FLUX PARAMETERIZATION.....	9
E.	UNCERTAINTIES IN SURFACE FLUX PARAMETERIZATION.....	10
1.	Instrumentation or Data Errors	11
2.	High or Low Wind Conditions.....	11
3.	Wave Boundary Layer and Effect of Waves	12
F.	SURFACE LAYER EM PROPAGATION AND DUCTING.....	13
G.	NEAR SURFACE MEASUREMENT PLATFORMS	17
H.	WAVE GLIDER / SHARC OVERVIEW.....	19
1.	Airmar PB200WX.....	22
2.	Existing Datasets of SHARC/Airmar Measurements.....	24
a.	<i>LRI PacX Measurements</i>.....	25
b.	<i>Datasets by NAVO SHARC Deployments</i>	25
III.	SHARC INSTRUMENTATION AND TESTING.....	27
A.	DEVELOPMENT OF CUSTOMIZED METOC PAYLOAD FOR SHARC.....	27
B.	NPS SHARC SENSORS.....	31
1.	Rotronic Model MP100H Temperature/Humidity Probe.....	31
2.	Vaisala Weather Transmitter WXT520.....	32
3.	Campbell Scientific Temperature Probe 109SS.....	32
4.	Garmin GPS 16-HVS.....	32
5.	True North Revolution Technologies GS Compass	32
6.	VectorNav VN-100 Rugged Accelerometer	33
C.	FIELD TESTS OF NPS SHARC INSTRUMENTATION	33
1.	Static Intercomparison	33
2.	At-Sea Testing	34
a.	<i>MASFlux Configuration</i>	34
b.	<i>Deployment and Recovery Procedures</i>.....	37
IV.	NPS MET SENSOR PERFORMANCE AND AIRMAR EVALUATION.....	39
A.	NPS MET PAYLOAD EVALUATION	39
1.	Wind Speed and Direction Measurements	39
2.	Specific Humidity.....	44
3.	Pressure.....	46

4.	Temperature	47
5.	Solar Heating Effect.....	50
6.	NPS Met Mean Measurement Conclusions	53
B.	NPS TESTING AND EVALUATION OF THE AIRMAR.....	53
1.	NPS Airmar at Sea Testing	53
2.	NPS Airmar Static Testing.....	56
C.	EVALUATION OF AIRMAR MEASUREMENTS COLLECTED BY LRI AND NAVO SHARCS.....	59
1.	PacX SHARC Data	59
2.	NAVO SHARC Airmar Data Analysis	65
3.	Airmar Data Set Conclusions and Statistics.....	70
V.	EXAMPLE OF SHARC-BASED NEAR SURFACE MEASUREMENT FOR NAVAL APPLICATIONS	73
A.	SURFACE FLUX.....	73
B.	NEAR SURFACE PROFILES AND EDH CALCULATIONS.....	76
VI.	CONCLUSIONS AND RECOMMENDATIONS.....	79
A.	SHARC, NPS MET, AND AIRMAR CONCLUSIONS	79
B.	RECOMMENDATIONS FOR FUTURE WORK.....	80
	LIST OF REFERENCES.....	81
	INITIAL DISTRIBUTION LIST	85

LIST OF FIGURES

Figure 1.	A schematic of the air-sea interface processes (from Woods Hole Oceanographic Institution [WHOI] 2011)	6
Figure 2.	Categories of radar propagation based on refractive index (from Turton et al. 1988).	14
Figure 3.	Typical M profiles resulting in ducts (from Babin et al. 1997).	15
Figure 4.	Near neutral condition sensitivity to mean measurement inputs (from Twigg 2007).	16
Figure 5.	MASFlux Buoy deployment.	18
Figure 6.	Illustration of main components of SHARC (from Rochholz 2010).	19
Figure 7.	Illustration of how the wave glider converts wave-powered vertical motion into forward motion (from LRI 2012a).	20
Figure 8.	Illustration of the Wave Glider’s modular payload dry boxes (from LRI 2012a).	21
Figure 9.	Airmar PB200WX weather station mounted on the SHARC.	23
Figure 10.	NAVO SHARC track as it orbited NDBC buoy 51002 in April 2012 (from Wang 2012).	26
Figure 11.	NPS customized METOC sensor suite mounted on the SHARC.	28
Figure 12.	Open aft payload bay, with dry box and data logger shown.	30
Figure 13.	Static testing of the Airmar PB200WX and the NPS sensor package a) atop a six floor building and b) at Fort Ord, Marina, CA.	34
Figure 14.	SHARC and MASFlux tracks during at-sea field testing.	36
Figure 15.	Time variation of the MASFlux and NPS Met wind speed measurement on a) July 29, 2014; b) July 30, 2014; c) August 8, 2014.	41
Figure 16.	Comparison of the level one MASFlux wind speed measurements and the NPS Met wind speed measurements during at sea testing.	42
Figure 17.	Same as Figure 15, except for wind direction.	43
Figure 18.	Same as Figure 16, except for wind direction.	43
Figure 19.	Same as Figure 15, except for specific humidity.	45
Figure 20.	Same as Figure 16, except for specific humidity.	45
Figure 21.	Same as Figure 15, except for pressure.	46
Figure 22.	Same as Figure 16, except for pressure.	47
Figure 23.	Same as Figure 15, except for temperature.	49
Figure 24.	Same as Figure 16, except for air temperature.	50
Figure 25.	Relationship of the solar heating of the multi-plate radiation shield used on the Rotronic sensor to the ventilation rate and sun angle (from R. M. Young, 2012.)	51
Figure 26.	Typical measurements of NPS Met temperature, incoming solar irradiance, and wind speed at Fort Ord during the intercomparison testing on a sunny day.	52
Figure 27.	Same as Figure 26, except for a cloudy day.	52
Figure 28.	Time variation of Airmar and NPS Met pressure measurements during at sea testing on a) July 29, 2014; b) July 30, 2014; c) August 8, 2014.	54

Figure 29.	Comparison of the Airmar pressure measurements versus the NPS Met pressure measurements during at-sea testing.	55
Figure 30.	Time variation of Airmar and NPS Met wind speed measurements during at sea testing on a) July 29, 2014; b) July 30, 2014; and c) August 8, 2014; and time series plots of wind direction measurements on d) July 29, 2014 e) July 30, 2014 and f) August 8, 2014.	55
Figure 31.	Same as Figure 29, except for a) wind speed; b) wind direction.	56
Figure 32.	Time variation of Airmar 1 Hz measurements during static testing where blue and red indicates NPS Met and Airmar measurements, respectively.	57
Figure 33.	Comparison of 10 minute averaged static Airmar and NPS Met measurements for a) pressure; b) air temperature; c) wind speed.	58
Figure 34.	SHARCs 1, 2, and 4 path during November, 2012 PacX. The inner box shows tracks within 15 km of buoy 46092.	60
Figure 35.	Time variation of the PacX SHARC and buoy 46092 pressure measurements.	61
Figure 36.	Comparison of the LRI SHARC and NDBC pressure measurements.	61
Figure 37.	Same as Figure 35, except for a) wind speed; b) wind direction measurements.	62
Figure 38.	Same as Figure 36, except for a) wind speed measurements; b) wind direction measurements.	63
Figure 39.	Same as Figure 35, except for air temperature.	63
Figure 40.	Same as Figure 36, except for air temperature measurements.	64
Figure 41.	Comparison of the LRI PacX SHARC and NDBC buoy 46092 measured air temperature with a) daytime data in red and nighttime data in blue; b) when wind speed was less than 2 ms^{-1} (circled in green) to examine the effects of solar heating on the Airmar.	65
Figure 42.	NAVO SHARC tracks within 15 km of buoy 46092 from September – December 2012 in Monterey Bay. Location of Buoy 46092 is shown in green on the horizontal axis.	66
Figure 43.	Time variation plot of the NAVO SHARC Airmar and NDBC buoy 46092 wind directions from the entire intercomparison mission between September and December 2012.	66
Figure 44.	Comparison of the NAVO SHARC and NDBC buoy 46092 wind direction measurements.	67
Figure 45.	Time variation of the NAVO SHARC and NDBC buoy 46092 measurements with a) wind speed centered around October 1, 2012; b) wind speed centered around November 1, 2012; c) pressure centered around October 1, 2012; d) pressure centered around November 1, 2012.	68
Figure 46.	Comparison of the NAVO SHARC and NDBC buoy 46092 a) wind speed measurements; b) pressure measurements.	68
Figure 47.	Same as Figure 45, except for air temperature.	69
Figure 48.	Same as Figure 41, except for the NAVO SHARC.	69
Figure 49.	Time variation of NPS Met and MASFlux surface fluxes derived using mean measurements and COARE, and the fluxes from the EC method on a) July 29, 2014; b) July 30, 2014; c) August 8, 2014.	74

Figure 50.	Comparison of NPS Met momentum flux derived using mean measurements and COARE, and the momentum flux from the EC method. ..75
Figure 51.	Same as Figure 50, except for virtual sensible heat flux.75
Figure 52.	Example vertical profiles derived using SHARC measurements from August 8, 2014 at-sea testing and the output of COARE algorithm.....77
Figure 53.	EDH and EDS calculated from the SHARC derived near surface vertical profiles during August 8, 2014 at-sea testing.78

THIS PAGE INTENTIONALLY LEFT BLANK

LIST OF TABLES

Table 1.	Bulk measurement precision requirements for EDH calculations (after Paulus 1989).....	16
Table 2.	Table Sensor and Instruments for LRI METOC gliders (after LRI 2012b). ...	22
Table 3.	Airmar PB200WX specifications (after Airmar 2011).....	24
Table 4.	NPS customized METOC sensor suite and measured variables.....	29
Table 5.	Manufacturer stated accuracy and ranges of the NPS customizer METOC sensors, GPS, accelerometer, and compass package.	31
Table 6.	One hour averages as reported by NDBC buoys at 1102 PDT on each deployment day.....	36
Table 7.	Statistical comparison of MASFlux and NPS Met measurements during at sea testings.	53
Table 8.	Statistical comparison of Airmar and NPS Met measurements using 10 minute averages of the 1 Hz raw data during November 2014 static testing.....	59
Table 9.	Statistical comparison between SHARC/Airmar at-sea environmental measurements and measurements from known, high quality instruments.	71

THIS PAGE INTENTIONALLY LEFT BLANK

LIST OF ACRONYMS AND ABBREVIATIONS

ABL	atmospheric boundary layer
AHRS	Attitude Heading Reference System
AREPS	Advanced Refractive Effects Prediction System
COAMPS	Coupled Ocean/Atmosphere Mesoscale Prediction System
COARE	Coupled Ocean-Atmosphere Response Experiment
EC	eddy correlation
EDH	evaporation duct height
EDS	evaporation duct strength
EM	electromagnetic
GOS	Global Observing System
IMU	Inertial Measurement Unit
LRI	Liquid Robotics, Inc.
MASFlux	Marine-Air-Sea-Flux
METOC	meteorological and oceanographic
MOST	Monin-Obukhov Similarity Theory
NAVO	Naval Oceanographic Office
NCOM	Navy Coastal Ocean Model
ONR	Office of Naval Research
NOAA	National Oceanic and Atmospheric Administration
NDBC	National Data Buoy Center
NPS	Naval Postgraduate School
PacX	Pacific Crossing
R/V	research vessel
SHARC	Sensor Housing Autonomous Remote Craft
SPAWAR	Space and Naval Warfare Systems Command
SST	sea surface temperature
TAWS	Target Acquisition Weapons Software
TOGA COARE	Tropical Ocean Global Atmosphere Coupled-Ocean Atmosphere Response Experiment
USV	unmanned surface vehicle

WBL wave boundary layer
WMO World Meteorological Organization

ACKNOWLEDGMENTS

I would be remiss if I did not thank the following individuals for their guidance and hard work in helping me to research and write this thesis. First, I want to offer my appreciation to Dr. Qing Wang who readily and generously shares her brilliance, insight, and time with her students. It was an absolute pleasure to work with Dr. Wang, and I feel very fortunate to have done so. I also want to say thank you to Mr. Dick Lind and Mr. Ryan Yamaguchi. Without their skill, knowledge, and countless hours of work, this thesis truly would not exist. Finally, I want to thank my husband who encouraged me to dedicate the time and energy necessary to strive for excellence in this master's program and thesis process. He kept our household and my sanity in check, and I am so very lucky to have him in my life.

THIS PAGE INTENTIONALLY LEFT BLANK

I. INTRODUCTION

A. IMPORTANCE OF NEAR SURFACE

Accurately quantifying the characteristics of the near surface environment is critical to understanding and modeling Earth's atmosphere. In particular, studying the near surface marine environment is especially important because oceans cover over 70 percent of the surface of the Earth. The exchanges of momentum, heat, moisture, and turbulence among the upper ocean, ocean surface, and lower atmosphere play an integral role in determining the dynamics of both the ocean and the atmosphere. Better theoretical representation and experimental examination of the interplay between the ocean and atmosphere are needed, which calls for a major systematic and well-organized observation program of the ocean and the structure of the atmospheric boundary layer (Kraus and Businger 1994). Obtaining research grade, high quality near ocean surface measurements, however, poses many challenges. A long endurance, mobile platform capable of observing the near surface environment would benefit many scientific fields.

Collecting in situ measurements of key variables that characterize the nonlinear air-sea interaction process, or an accurate representation of such processes, remains one of the greatest challenges to environmental forecast model improvement. For the exchanges of mass and energy across the air-sea interface, bulk aerodynamic surface flux parameterization schemes are needed, which are largely built upon the Monin-Obukhov similarity theory (MOST) developed in 1954 (Liu et al. 1979). Fairall et al. (1996b, 2003) further refined the bulk surface flux scheme using data collected during the Tropical Ocean Global Atmosphere (TOGA) Coupled Ocean-Atmosphere Response Experiment (COARE) that resulted in what is known as the COARE bulk flux algorithm. COARE is now the most widely used flux algorithm in most of the mesoscale and global scale forecast models. Limitations to the COARE algorithm do, however, exist, partly due to the inherent assumptions of MOST (e.g., Andreas et al. 2014). Thus, the need to collect high-quality data at the air-sea interface persists in order to further improve surface flux parameterization algorithms and hence forecast models.

Near-surface measurements are also important for developing and verifying coupled air-sea forecast models. Coupled air-sea models have produced improved results in certain conditions and demonstrate the potential for greater use (Powers and Stoelinga 1999). Coupled models are also critical for studying climate variability because the accurate parameterization of air-sea momentum and heat flux is critical for realistic simulation of the atmosphere-ocean system (Brown et al. 2013). Near surface data sets and observations are thus indispensable to fill in the need of developing and improving coupled forecast models.

Near surface measurements also provide critical validation of satellite data that provide broad global coverage of measurements, particularly in otherwise data sparse regions. Developing and refining remote sensing techniques, however, require in situ observations. Due to a lack of open ocean near surface measurements, many satellite validations over the ocean rely on climatology or bulk algorithms to convert ship or land-based measurements to near surface quantities. These data sets are not adequate to fully validate satellite retrieval methods over the open ocean, thus, more in situ observations are necessary (Waliser et al. 1999).

Similarly, electromagnetic (EM) propagation models also depend on robust in situ measurements and/or highly accurate forecasts. Surface moisture and temperature gradients affect the height of the evaporative duct that can act as a wave guide for high frequencies (Edson et al. 1999). EM propagation is very sensitive to the vertical variation in the atmospheric boundary layer (ABL) and would also benefit from improvements of model parameterizations with additional data for both research and operational purposes.

B. RESEARCH OBJECTIVES

A network of near surface, ocean observing platforms that are capable of providing high quality measurements would aid in furthering all of the studies described above. In 2012, NPS received two wave gliders, referred to by the Navy as “Sensor Housing Autonomous Remote Crafts” (SHARC). The goal of this thesis is to improve the quality and coverage of near surface observations available for Naval applications and surface flux research. Specifically, this thesis will present an evaluation of the SHARC as

a platform for gathering meteorological and oceanographic (METOC) data in general, and air-sea interface flux data in particular. Compared to other near shore platforms, the SHARC adds longevity, mobility, and the ability to “drive” to areas of interest. Measurements from the standard SHARC weather station sensors, as well as a newly developed suite of sensors, will be compared to those from research grade sensors on the NPS Marine Air-Sea Flux (MASFlux) buoy. Three co-deployments of the SHARC and the MASFlux buoy in Monterey Bay, and static tests of the SHARC standard instruments and NPS sensors, were conducted to provide the datasets for comparison. These datasets will also be used for surface flux parameterization analysis. Additionally, other SHARC users have provided measurements collected by the standard SHARC weather sensors. These groups have presented initial findings in Wang et al. (2012) and Griffith et al. (2012). This thesis will provide a more detailed examination of their datasets.

This thesis focuses on the testing and improvement of the SHARC and its environmental sensors. The ultimate goal of this thesis, however, is the utilization of SHARCs to provide high quality near surface data in sparse, hostile, or severe weather environments. The resulting data can then be used in applications as varied and important as protecting Naval assets and personnel from adverse weather, to achieving decision superiority in the electromagnetic spectrum.

C. NAVAL APPLICATIONS

The near surface environment plays a critical role in determining EM propagation, improving coupled model and severe weather forecasting, and in predicting wave dynamics and forecasts. As the Navy’s focus shifts from mainly blue water operations to also include more littoral regions, the complexity of the environment, forecasting requirements, and decision aids also increase. Rear Admirals White and Filipowski said in a recent *Proceedings* article, “[c]ollecting the raw data, processing and analyzing the data, and predicting how that data will change... assist operational commanders in making faster and better decisions than the adversary” (2014). According to a 1999 Office of Naval Research (ONR) report, the Navy requires increasingly accurate and detailed weather, wave, and ocean forecasts (Edson et al.). There is also mounting

interest in coupled models and forecasts. Near surface data are key to improving surface flux parameterization and understanding the mechanisms that couple the ocean and atmosphere. Additionally, real-time near surface observations are essential for model development and validation.

1. Electromagnetic Propagation

The most important and immediate applications of near surface measurements is for EM propagation studies and predictions. The Navy uses the EM spectrum for communication, radar detection and avoidance, and electronic warfare. As weapon systems and platforms become more complex, so does their dependence on EM propagation and control of the EM domain. EM performance predictions are therefore a Navy requirement. As Admiral Jonathan Greenert, Chief of Naval Operations, said,

The electromagnetic (EM) spectrum is an unseen but integral part of our daily personal lives. And, it is essential to our military operations. Failing to use it effectively WILL be the difference between victory and defeat. The EM environment presents us with challenges and opportunities in the 21st century. It is an area we can use to gain an advantage over our adversaries. To command it, we need the ability to monitor and be aware of the environment, manage our emissions, discretely communicate, find, track and defeat threats, and conduct attacks as needed. (2012)

As described above, EM propagation is very sensitive to even small changes in the ABL temperature and moisture gradients. Near surface measurements are critical to determining and accurately forecasting these gradients and the structure of the ABL. Advanced Refractive Effects Prediction System (AREPS) and Target Acquisition Weapons Software (TAWS), in particular, require accurate ABL profile inputs in order to effectively predict EM propagation, radar ranges, and weapon sensor effectiveness. In fact, Konstanzer (1994) found that a two meter change in the evaporation height duct (EDH) could cause a 50 percent change in the SPY-1 radar detection range. Both in situ near surface measurements, and improved parameterization equations will improve the Navy's EM performance prediction capability.

II. BACKGROUND

The interaction between the atmosphere and the ocean at the air-sea interface is dynamic, complex, and non-linear. This interaction, and the associated exchange of momentum, energy, and mass across the air-sea boundary, determines the structure of the lower atmosphere and upper ocean. These processes, while critical to many scientific fields as described in Chapter I, remain difficult to measure or study directly.

Surface flux parameterizations seek to model these air-ocean exchanges. A further extension of the surface flux parameterization is to calculate near surface profiles when in-situ measurements of fluxes and profiles with sufficient vertical resolution are not available. The state-of-art COARE algorithm, validated by a large amount of over-ocean datasets, has been broadly used by nearly all mesoscale forecast models as well as models at smaller or larger scales. Combining with MOST, it is also used to derive surface layer profiles for applications such as EM propagation and ducting over the ocean. In this study, deduction of surface flux and surface layer vertical profiles from the SHARC measurements will also continue to utilize MOST and COARE.

A. PHYSICAL PROCESSES AT THE AIR-SEA INTERFACE

The ocean-atmosphere exchange consists of many dynamic and interwoven processes, as shown in Figure 1. At the heart of this interaction are the turbulent exchanges of momentum, sensible and latent heat, which drive turbulent mixing in the atmospheric boundary layer. Such turbulent mixing, combined with entrainment at the top of the boundary layer, modifies the near-surface wind, temperature, and specific humidity, and hence feedback to air-sea exchange processes. The air-sea momentum and energy transfer is thus a coupled process. On the upper ocean side, wind-driven surface stress, sensible and latent heat fluxes, and atmospheric radiation result in upper ocean turbulent mixing that modifies the sea surface temperature. Wind generated waves and swells are also part of the equation in these coupled processes to modify the surface roughness. The wave breaking creates aerosols and sea spray that affect the turbulent heat transfer and the absorption and reflection of radiation. Changes in radiation and heating

also affect precipitation, which, in turn, may modify the wind and thermodynamics of the subcloud layer through evaporative cooling. On the larger scale, these air-sea processes drive open ocean circulation and determine the mixed layer depth. Within the atmosphere, these processes determine the structure of the lower atmosphere. Understanding near surface physical processes is therefore critical to modeling and predicting the coupled air-ocean environment.

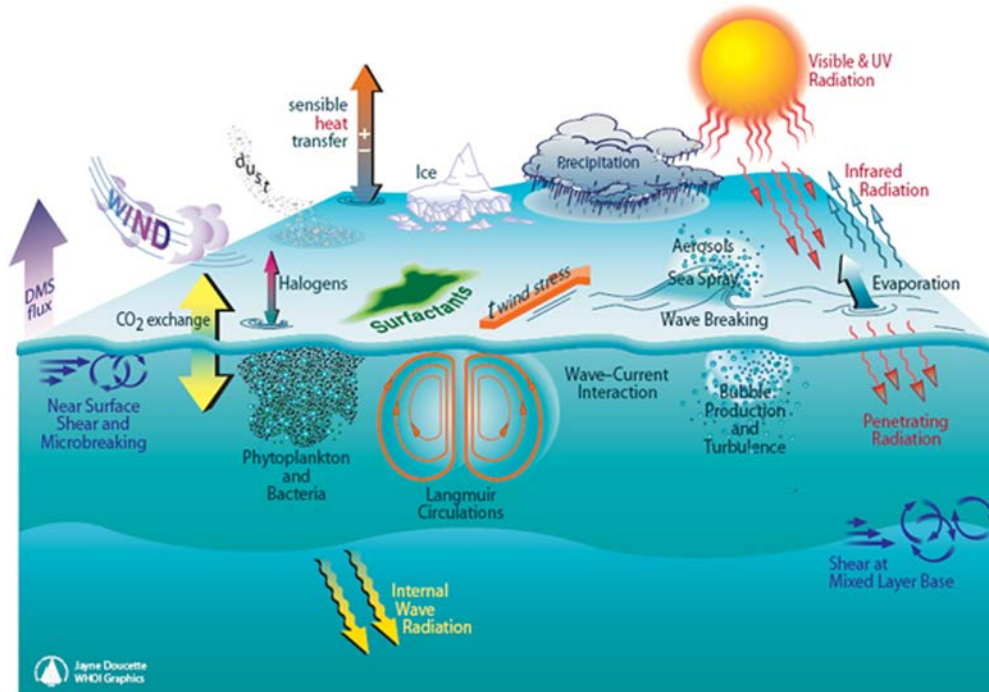


Figure 1. A schematic of the air-sea interface processes (from Woods Hole Oceanographic Institution [WHOI] 2011)

B. SURFACE FLUX

The energy, mass, and momentum exchange between the atmosphere and the ocean physically couple the two media. The amount of exchange of a quantity across a unit area is called, “flux.” Flux occurs as a result of flow perpendicular to and through the interface. For example, the amount of flux (F_x) for a variable x through a horizontal plane by the vertical wind, w , could be shown by

$$F_x = \overline{wx} \quad (1)$$

The flow and the entity being examined then can be broken into mean (denoted by the overbar) and perturbation (denoted by the prime) portions using Reynolds decomposition.

$$F_x = \overline{wx} = \overline{(\overline{w} + w')(\overline{x} + x')} = \overline{w \cdot x} + \overline{w' x'} \quad (2)$$

The first term on the right-hand-side of Eqn. (2) is referred to as the advective flux caused by the mean flow of a fluid, while the second term is a result of turbulent or perturbation flow and is referred to as the eddy flux or turbulent flux. For the horizontal plane, the mean vertical velocity is generally small, thus reducing the total flux to turbulence flux only.

$$F_x = \overline{w' x'} \quad (3)$$

One can then use the eddy correlation method to calculate vertical turbulent flux of a quantity as the covariance of the perturbations in vertical wind velocity and the perturbations in the desired entity at a point (Readings et al. 1969). With sufficiently fast sampling instruments, this correlation method allows for direct turbulence flux measurements.

The most important fluxes between air and sea at the interface are the vertical exchange of momentum (τ), sensible heat (H_s), and latent heat (H_l). These fluxes can now be represented by scaling parameters defined by the following equations:

$$\begin{aligned} \tau &= \rho(\overline{w'u'^2} + \overline{w'v'^2})^{1/2} = u_*^2 \\ H_s &= \rho C_p \overline{w'\theta'} = -\rho C_p u_* \theta_* \\ H_l &= \rho L_v \overline{w'q'} = -\rho L_v u_* q_* \end{aligned} \quad (4)$$

where ρ is the dry air density, u' , v' , w' are the horizontal and vertical wind components; C_p is the specific heat capacity of air at constant pressure; L_v is the latent heat of vaporization; θ is air potential temperature; the prime indicates perturbations; the overbar indicates the time average; and the '*' subscript indicates the respective quantity surface layer turbulence perturbation scale.

Direct measurements of fluxes and their governing turbulent processes are difficult to obtain operationally. These exchanges happen on small scales and require

high-rate sampling so that the small scale turbulent perturbations can be resolved. Therefore, calculating flux by using more easily obtained mean profile measurements is critical to modeling the environment and the numerous applications described in Chapter I. This concept is the basis for surface flux parameterization.

C. MONIN-OBUKHOV SIMILARITY THEORY (MOST)

In the lowest 10 percent of the atmospheric boundary layer, Coriolis is negligible and flux remains nearly constant with height (Businger et al. 1971). This layer is called the surface layer and is approximately 50–100m in height. In this layer, the primary sources for generating turbulence are buoyancy and wind shear. Monin and Obukhov (1954) used this concept, combined with dimensional analysis, to derive the relationship between the mean wind, temperature, and specific humidity profiles to surface turbulent fluxes. The resultant non-dimensional gradients can be expressed as:

$$\begin{aligned}\frac{\kappa z}{u_*} \frac{\partial \bar{u}}{\partial z} &= \phi_m \left(\frac{z}{L} \right) \\ \frac{\kappa z}{\theta_*} \frac{\partial \bar{\theta}}{\partial z} &= \phi_h \left(\frac{z}{L} \right) \\ \frac{\kappa z}{q_*} \frac{\partial \bar{q}}{\partial z} &= \phi_h \left(\frac{z}{L} \right)\end{aligned}\tag{5}$$

where von Karman's constant $\kappa \approx 0.35-0.40$ derived from measurements, L is the Monin-Obukhov length: $L = \frac{u_*^3 \theta}{\kappa g w' \theta'}$, g is gravity, z is height, and $\phi_m(\frac{z}{L})$ and $\phi_h(\frac{z}{L})$ are non-dimensional universal functions that account for the thermal stability of the surface layer.

The left hand side of the equations is the non-dimensional vertical gradient of mean wind, mean potential temperature, and mean specific humidity. The right hand side of the equations indicates that these mean gradients are functions of height non-dimensionalized by L , denoting the effects of thermal stability. When the surface layer is neutral, the universal function for momentum is equal to one. The other universal function values have been determined by experiment. Businger et al. (1971) derived their widely used land-based universal functions in the famous 1968 Kansas experiment.

The MOST non-dimensional functions provide the link between bulk, mean profiles and turbulence measurements. This relationship developed by Monin and Obukhov serves two primary functions. First, MOST allows researchers or models to calculate surface layer turbulent fluxes using of mean profile measurements. This procedure is especially important when fast turbulence direct sampling is not possible. MOST also allows researchers to calculate mean wind at a level at which they did not take direct observations. For example, many flux parameterization equations require mean winds at 10m. By using the non-dimensional gradient, known mean values at one level, and surface flux values, researchers can compute the wind at 10m. Finally, if observations are available at only one level and flux is unknown, both the gradient and the surface turbulent fluxes can be derived by using the surface roughness height and assumed mean properties at the roughness length. The surface roughness height (z_0) is the height at which mean wind is zero (Charnock 1955). Similarly, the air temperature at the surface roughness height is set equal to SST, and the specific humidity over salt water at the surface roughness height is defined as 98 percent.

MOST does, however, have limitations and researchers continue to refine the universal function values and debate the conditions under which MOST is valid (Foken 2006). MOST assumes horizontally homogenous conditions that may not hold true near the coast or near a front (Cheney 2011). Additionally, MOST assumes that the constant flux layer is in equilibrium with the surface which may not hold true over rough surfaces (Foken 2006). For naval and marine applications, there are also questions as to whether the Businger universal functions derived over-land are also valid over water.

D. SURFACE FLUX PARAMETERIZATION

Surface flux algorithm calculates surface turbulent fluxes using bulk, mean measurements because bulk, mean quantities are more readily sampled or forecast by numerical models. Per Fairall et al. (2003), turbulent flux parameterizations usually use a bulk transfer coefficient. For example, the flux of a variable x would be

$$F_x = \overline{w'x'} \approx C_x S \Delta X \quad (6)$$

where C_x is the bulk transfer coefficient, S is the mean wind speed relative to the ocean surface, and ΔX is the difference in the mean value of x from the sea to the air. The standard bulk expressions for the primary air-sea surface fluxes are then

$$\begin{aligned}\tau &= \rho C_d S (U_s - U) \\ H_s &= \rho C_p C_h S (T_s - \theta) \\ H_l &= \rho L_v C_e S (q_s - q)\end{aligned}\tag{7}$$

where C_d , C_h , and C_e are the total transfer coefficients for wind stress, sensible heat, and latent heat, respectively; the subscript ‘s’ represents the value at the air-sea interface. The representation of the drag and exchange coefficients are the key of this parameterization algorithm.

Building on the foundation of MOST and the Businger universal function parameterizations, the Tropical Ocean Global Atmosphere Coupled-Ocean Atmosphere Response Experiment (TOGA COARE) added ocean based observations to the flux database and refined the bulk flux parameterization (Fairall et al. 1996b). The researchers used these simultaneously collected bulk and flux measurements to refine bulk algorithms and the associated transfer coefficients, roughness parameter, and universal functions. Their modifications attempted to account for light winds, cooling effects of precipitation, and convection (Fairall et al. 1996b). The COARE parameterizations and their subsequent revisions are currently widely used by air-sea researchers and coupled forecast models (Fairall et al. 2003). The analysis presented in this thesis will utilize the COARE algorithm to obtain surface fluxes and near-surface mean profiles.

E. UNCERTAINTIES IN SURFACE FLUX PARAMETERIZATION

According to Bao et al. (2002), there are two main sources of uncertainty for sea-air fluxes. The first type of uncertainty derives from uncertainty in the observational data and measurements, themselves. The second major source of uncertainty results from questions of when MOST is valid. In particular, there remain questions about how well MOST performs in conditions with very high or low winds, waves and swells, and different surface layer stabilities.

1. Instrumentation or Data Errors

Measurements of the bulk and turbulent near surface quantities continue to pose challenges in terms of how the observations are gathered, used, and analyzed. Tsvang et al. (1973) note the importance of instrument intercomparisons to ensure near surface measurement accuracy. In their series of turbulence measurement experiments, Tsvang et al. (1973) note that “the influence of instrumentation and analysis on the results is often subtle and complicated so that it may not be readily detected, let alone removed.” For example, different research groups have obtained different values for universal functions and parameterizations. These differences, however, may result from differences in measurement method or quality, rather than inadequacies of the underlying theory (Tsvang et al. 1973). Instrument intercomparisons help to eliminate some of these uncertainties and potential sources of error.

SST measurements are very difficult, if not impossible, to obtain exactly at the interfacial surface. In addition to flow disturbance caused by the instruments and observation platforms, the warm layer and cool skin effect described in Fairall et al. (1996a) affects the ability to obtain accurate interfacial temperature measurements. The warm layer results when solar radiation warms the upper few meters more than it heats the deeper mixed layer. The cool skin results from a combination of net longwave radiation and heat flux that cools the upper few millimeters more than it cools the layer beneath it. Thus, depending on where in the water column SST is measured, in situ measurements may need to be adjusted for further analysis or use in parameterization equations.

2. High or Low Wind Conditions

There are questions as to whether MOST and the algorithms derived from that theory remain valid in very high or very low wind conditions. MOST and the bulk aerodynamic algorithms derived from MOST show that the drag coefficient, C_d , should increase with wind speed over the water (Zhu and Furst 2013). In very low winds, however, observations show that C_d actually increases with a decrease in wind speed (Zhu and Furst 2013). In very high winds, spray conditions also affect heat fluxes. Total

sensible and latent heat fluxes are actually composed of interfacial fluxes, which are accounted for in COARE, and fluxes on the surface of sea spray droplets which are not accounted for in COARE (Andreas et al. 2008). For wind speeds over 10 ms^{-1} , the spray fluxes become a significant fraction of the overall flux and cannot be neglected (Andreas et al. 2008).

3. Wave Boundary Layer and Effect of Waves

According to Edson and Fairall (1998), “the use of overland measurements to infer surface fluxes over the open ocean raises questions about the universality of these relationships.” Specifically, Edson and Fairall (1998) theorize that wave-induced effects in the wave boundary layer (WBL) can create conditions where turbulent fluxes do not dominate total fluxes. Rutgersson et al. (2001) explain that the WBL is the layer at the ocean surface that is directly affected by waves, and in which the surface roughness height, z_o , changes as the waves evolve. Charnock (1955) derived a relationship for the surface roughness length as

$$z_o = \alpha_c \frac{u_*^2}{g} \quad (8)$$

where α_c is a constant called the Charnock parameter; u_* is frictional velocity, and g is the gravitational acceleration. As winds increase, waves and the surface momentum flux in the WBL also increase. Thus, per the Charnock (1955) equation, the surface roughness height in the WBL is dependent on the wind and wave fields. According to Rutgersson et al., “As the waves evolve, the surface roughness changes, so the flow over the surface is coupled to the evolution itself” (2001). The so-called sea-state dependent parameterizations attempts to account for this changing surface roughness and relationship to wave age and wave steepness. Edson and Fairall (1998) do conclude, however, that MOST is valid over the ocean for measurements and calculations above the WBL.

F. SURFACE LAYER EM PROPAGATION AND DUCTING

Another important application of quality, near surface mean measurements is for use in EM propagation prediction. EM propagation paths depend on the refractive structure of the surface layer as determined by vertical temperature and humidity gradients. Modified refractivity, M , describes this structure while also taking into account the curvature of the earth. The modified refraction index, M , can be given by:

$$M = N + 0.157z = \frac{77.6}{T} \left(p + \frac{4810e}{T} \right) + 0.157z \quad (9)$$

where $N = \frac{77.6}{T} \left(p + \frac{4810e}{T} \right)$ is the radio refractivity index; p is the total atmospheric pressure; T is the air temperature in Kelvin; and e is the water vapor pressure in millibar. There are four general propagation path types defined by the vertical gradient of M : sub-refraction, standard refraction, super-refractions, and ducting. Figure 2 shows the four propagation types and their respective modified refractive gradients. The ducting conditions in which rays are bent downward or “trapped” when $dM/dz < 0$, are of particular interest for Naval applications. When EM waves become trapped in the ducting layer, the duct acts as a waveguide and leads to decreased propagation loss and extended radar ranges.

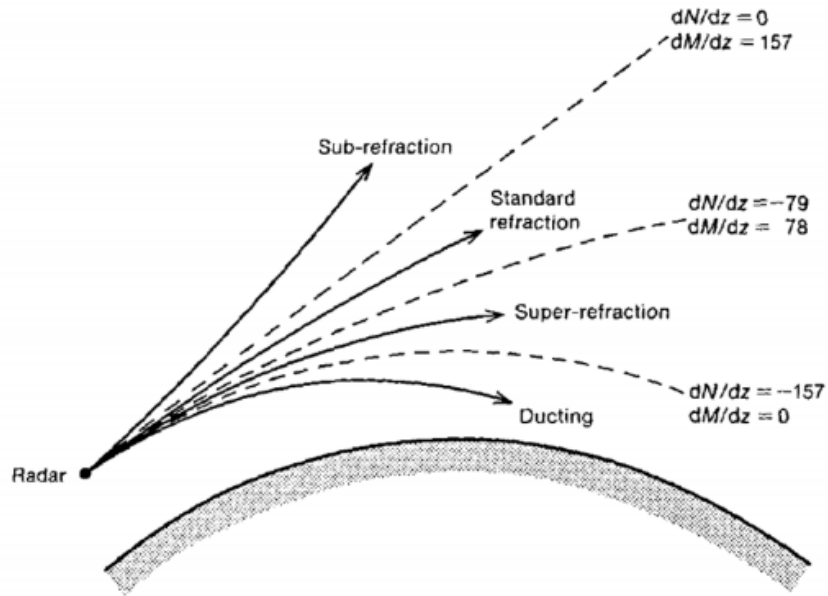


Figure 2. Categories of radar propagation based on refractive index (from Turton et al. 1988).

Evaporation ducts are a specific type of surface ducts that form over the ocean due to a steep decrease in humidity or increase in temperature with height (Ziemba 2013). Evaporation ducts often occur in areas where there is a temperature inversion combined with a significant decrease in moisture as height increases (Ziemba 2013). Figure 3(f) shows the M profile resulting in a typical evaporation duct.

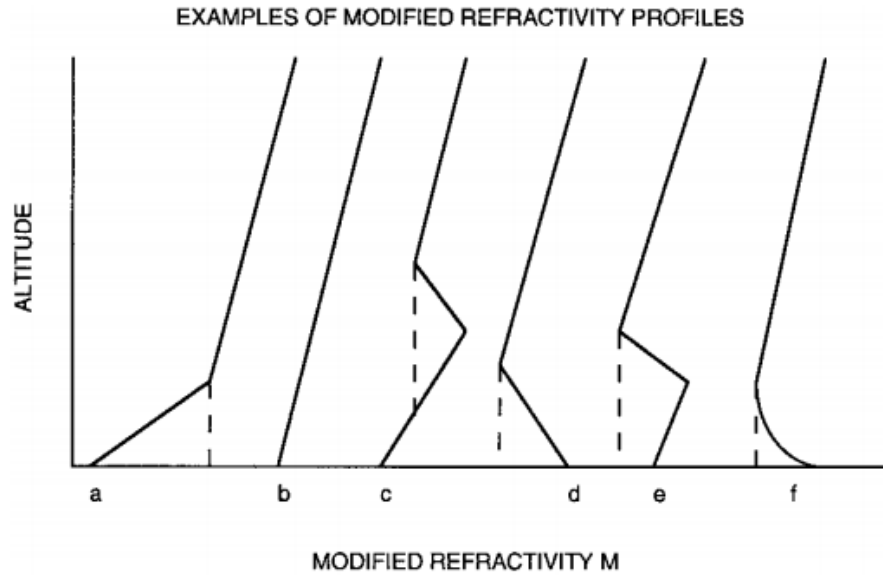


Figure 3. Typical M profiles resulting in ducts (from Babin et al. 1997).

The strength of the evaporative duct is related to the evaporation duct height (EDH). The EDH is defined as the height where the vertical gradient of the modified refractivity changes from negative to positive. As Paulus (1989) explains, the EDH “is not a height below which an antenna must be located to give extended ranges but rather a parameter indicative of the strength of the evaporation duct.” Typical ranges for the EDH are 0–40m. A high EDH indicates a strong evaporative duct that can trap lower frequencies, while a lower duct indicates a weak evaporative duct that can only affect higher frequencies (Paulus 1989).

Although ideally one would measure refractivity and EDH directly, it is not feasible on a large scale. Therefore, researchers have developed models based on bulk measurements and MOST to calculate the EDH (Babin et al. 1997). The primary factors that determine the EDH are SST, air temperature, relative humidity, wind speed, and the height of the measurements. The EDH models are sensitive to the bulk measurement inputs, especially in near-neutral stability conditions (Edson et al. 1999). Figure 4 shows the output of the NPS EDH model developed by Frederickson in 2007. In near-neutral conditions (air temperature approximately equal to the underlying SST), small

differences in wind speed led to very large changes in EDH. Table 1 lists the Paulus (1989) bulk measurement precision requirements for EDH calculations.

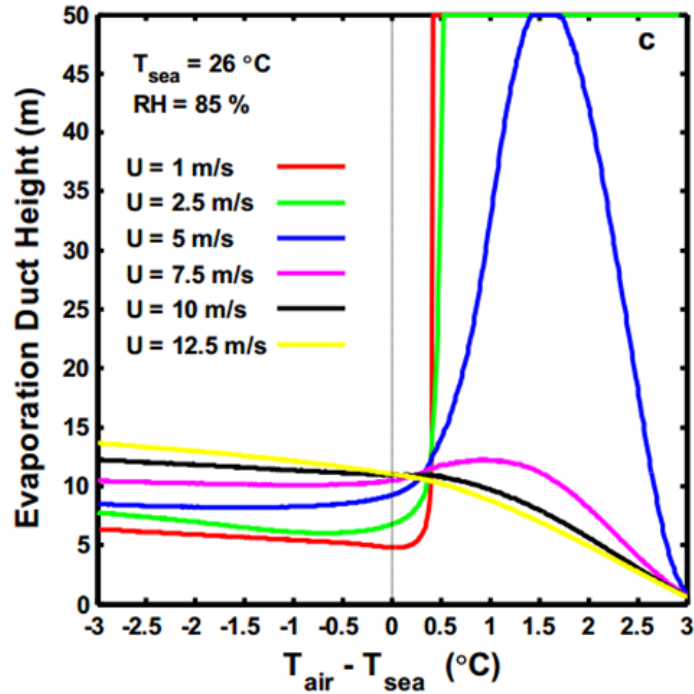


Figure 4. Near neutral condition sensitivity to mean measurement inputs (from Twigg 2007).

Parameter	Type	Precision
Wind speed	input	1 kt
Air Temp	input	0.1 C
RH	input	1%
SST	input	0.1 C
EDH	output	0.1 m

Table 1. Bulk measurement precision requirements for EDH calculations (after Paulus 1989).

G. NEAR SURFACE MEASUREMENT PLATFORMS

While platforms such as ships, fixed buoys, and flux buoys already do exist for collecting near surface observations, each presents challenges or limitations. Measuring air-sea wave and flux directly has proven difficult for many practical reasons. Per Edson et al. (1998), “problems usually arise from three sources: platform motion, flow distortion, and environmental factors unique to the ocean.” Ship-based measurements are usually obtained from an elevated level above the sea surface, and further suffer from flow distortion introduced by ship superstructures. As described above, satellite remote sensing introduces too many assumptions imbedded in data retrieval. NOAA NDBC buoys provide only mean measurements, are costly to maintain, and are fixed in location. The most ideal platform for obtaining flux measurements are flux buoys, which are normally large and heavy (~2000 lb), however. Deployment and recovery of these buoys is difficult and costly. Additionally, these buoys usually require complex mooring in deep waters.

Taking advantage of recent development in sensor miniaturization, especially in the inertial motion sensing, the Naval Postgraduate School (NPS) Meteorology Department developed the Marine-Air-Sea-Flux (MASFlux) buoy (Zuniga 2013). The MASFlux buoy is an instrumented spar-buoy, which is easy to deploy and recover, and does not distort the flow or temperature characteristics of the surrounding water (Figure 5). This system measures turbulent perturbations, mean wind and thermodynamic variables at multiple levels, 2-dimensional surface wave spectra, and upper ocean temperature simultaneously. The small buoy is not suited for deployment longer than a few days, however, and may not be operable in harsh conditions such as strong winds ($> 15 \text{ ms}^{-1}$) and high seas. A detailed description of the NPS MASFlux system can be found in the thesis work by Zuniga (2013).

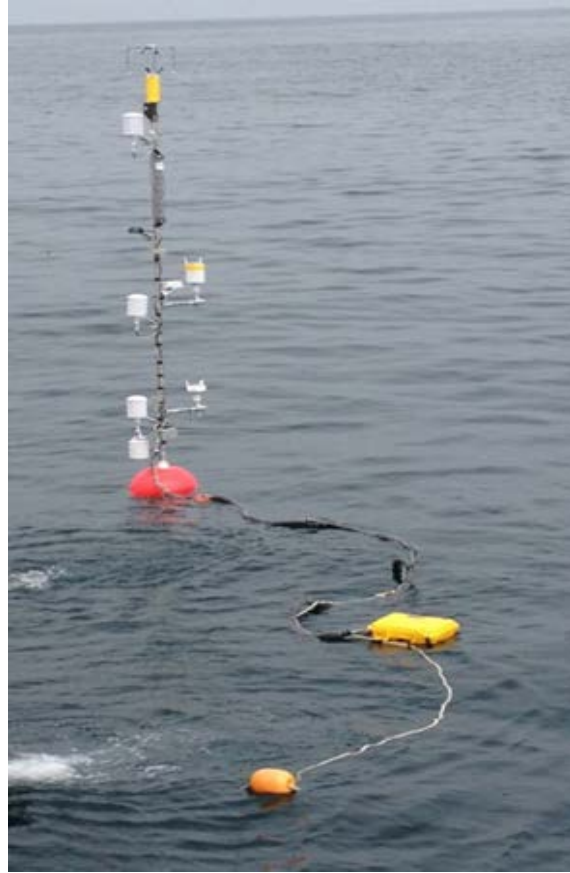


Figure 5. MASFlux Buoy deployment.

In addition to the limitations of each of the systems described above, the current instrument suites do not provide truly global coverage for near surface observations. The World Meteorological Organization's (WMO) Global Observing System (GOS) relies on approximately 11,000 stations to provide meteorological measurements at least every three hours. Many of these stations, however, are land based and there remain many data sparse regions, especially in the open ocean and in the Southern Hemisphere. For forecast models in particular, errors that arise in data-sparse regions are difficult to identify or diagnose. Not only do these coverage gaps reduce accuracy in those regions, but errors may propagate downstream to data-rich regions as well (Mathur et al. 1993). Additionally, climate change researchers require accurate ocean-atmosphere flux data and there are only limited observations in polar regions where heat and momentum exchanges are known to be particularly high (WHOI 2011).

H. WAVE GLIDER / SHARC OVERVIEW

Liquid Robotics, Inc (LRI), a Sunnyvale, California (CA) based company, introduced the Wave Glider in 2007. The Wave Glider is an autonomous, wave-propelled unmanned surface vehicle (USV) with a two-body design. When used by the Navy, the Wave Glider is known as the Sensor Hosting Autonomous Remote Craft (SHARC). The SHARC derives its power from wave and solar energy and, therefore, it provides a long-endurance and long-range platform for a variety of applications.

The SHARC consists of two main portions, an upper “float,” which rides on the surface of the water, and a lower “sub,” which is tethered approximately seven meters below the “float” via a flexible umbilical (Figure 6). The float and sub work in tandem converting the wave action energy in the ocean into forward propulsion. As the float rises and falls with the wave motion at the surface, the sub portion which resides in relatively stationary water seven meters below the surface, uses rotating “wings” to convert some of the vertical motion into forward thrust (Figure 7). In one to three foot seas, the SHARC maintains an average speed of 1.5 kts and up to one year of endurance (Hine et al. 2009).



Figure 6. Illustration of main components of SHARC (from Rochholz 2010).

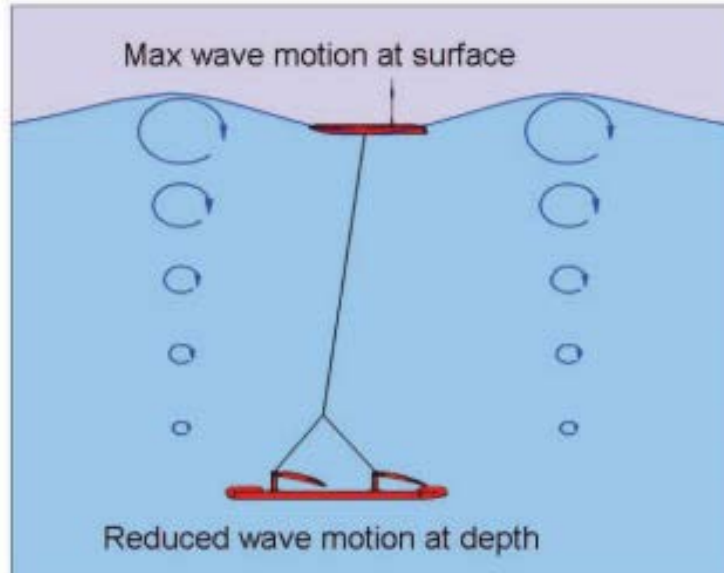


Figure 7. Illustration of how the wave glider converts wave-powered vertical motion into forward motion (from LRI 2012a).

Also enabling the SHARC's long endurance, is its use of solar power and rechargeable batteries to power its communications, navigation system, and additional payloads. On average, the SHARC can provide 10 watts of continuous power to its modular payloads (Hine et al. 2009). Communicating with the SHARC via an Iridium Satellite Modem and shore-based server, an operator can monitor the status of the wave glider and instruments, receive small packets of data, and input course adjustments. The operator can also prioritize power usage, as necessary, by dictating which sensors are on or off. All of these aspects have proven important when the SHARC is operating in hazardous weather conditions (Griffith et al. 2012).

Originally intended as a platform for listening to whales (Rochholz 2012), the Wave Glider can also be used as a sea-going platform to make measurements of the air-ocean environment. In fact, one of the most attractive features of the SHARC is its capacity to deploy different payloads based on the mission objectives. The SHARC float contains modular electrical interfaces and two open bays (Figure 8) for additional payload sensors and batteries.

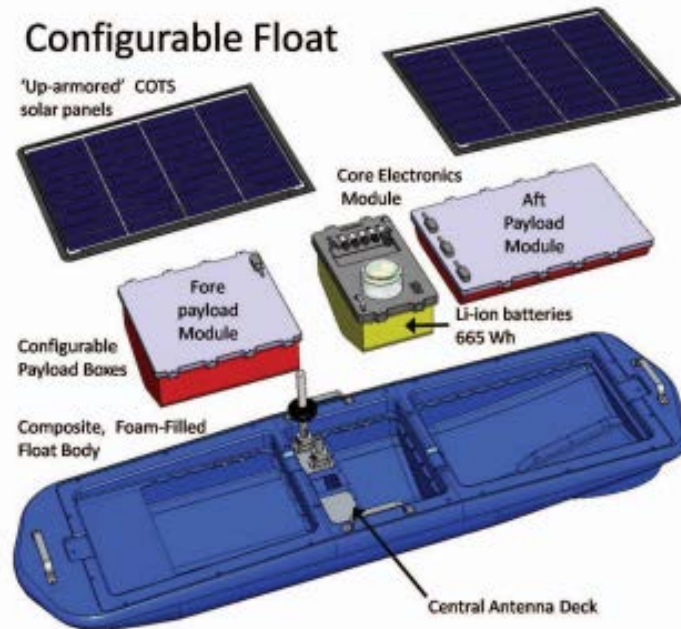


Figure 8. Illustration of the Wave Glider’s modular payload dry boxes (from LRI 2012a).

In addition to the open payload bays, LRI offers both the basic “METOC” and the “METOC Plus” models of the SHARC with built-in, integrated weather sensors (Table 2). The basic LRI METOC Wave Glider model uses the AIRMAR PB 200 to gather wind speed and direction, air temperature, and barometric pressure. The expanded LRI model (METOC Plus) adds wave and water sensors. The Datawell MOSE-G GPS-based directional wave sensor allows the SHARC to measure 2-dimensional wave spectra, wave height, propagation direction, and period, while the Sea-Bird GPCTD allows the SHARC to measure water temperature and salinity. Most LRI gliders acquired by Navy laboratories and centers (e.g., NAVO and SPAWAR) for meteorology and oceanography applications are the METOC Plus model. Although flux instrumentation is not part of the METOC or METOC Plus package, the SHARC also has great potential as a platform for collecting surface flux measurements. The customizable payload bays of the SHARC mean that collecting METOC data and performing other missions are by no mean exclusive tasks.







Sensor	Model	Description	METOC	METOC Plus
	Airmar PB200WX Weather Station	Weather information (air temperature, wind speed & direction, and barometric pressure)	X	X
	Teledyne RDI Acoustic Doppler Current Profiler (ADCP)	Measurement of ocean currents at the surface and in bins to the sensor's maximum depth	X	X
	Datawell MOSE-G GPS-based Directional Wave Sensor	Wave height, direction, period and spectrum		X
  	Sea-Bird GPCTD + DO	Water salinity analysis through collection of conductivity, temperature and density; dissolved oxygen measurement		X

Table 2. Table Sensor and Instruments for LRI METOC gliders (after LRI 2012b).

1. Airmar PB200WX

The NPS SHARC, “Mako,” is a basic LRI METOC model and arrived at NPS equipped with the Airmar PB200WX Weather Station for near surface meteorological measurements. Figure 9 shows the Airmar PB200WX mounted on a 1.12 m mast at the center of the Mako float (Figure 9). A blowup of the Airmar PB200WX is shown in the same figure.



Figure 9. Airmar PB200WX weather station mounted on the SHARC.

The PB200WX weather station measures air temperature, apparent wind speed and direction, and barometric pressure. Using an internal compass and GPS, the PB200 can also calculate true wind speed and direction (PB200 tech manual). Table 3 shows the manufacturer specifications of the Airmar PB200.

LRI preconfigures the Airmar for direct integration into the SHARC central data management system. Per this configuration, the Airmar PB200 sends data at specified intervals to the SHARC. At a one second interval, the PB200 sends the wind, pressure, temperature, and vehicle heading messages. At a 10 second interval, the PB200 transmits its GPS position and GPS time. The SHARC then averages the data over 10 minute intervals and, transmits the averaged observation to the WGMS server. The raw Airmar data, however, are neither stored nor transmitted to the WGMS server (Kirklin 2014, personal communication).

SPECIFICATIONS	
Wind Speed Range:	0 knots to 80 knots (0 MPH to 92 MPH)
Wind Speed Resolution:	0.1 knots (0.1 MPH)
Wind Speed Accuracy @ 0°C to 55°C (32°F to 131°F), no precipitation*:	
— Low Wind Speeds:	0 knots to 10 knots (0 MPH to 11.5 MPH); RMS error of 1 knot (1.1 MPH) +10% of reading
— High Wind Speeds:	10 knots to 80 knots (11.5 MPH to 92 MPH); RMS error of 2 knots (2.3 MPH) or 5% RMS, whichever is greater
Wind Speed Accuracy in wet conditions**:	5 knots (5.7 MPH) RMS
Wind Direction Range:	0° to 360°
Wind Direction Resolution:	0.1°
Wind Direction Accuracy @ 0°C to 55°C (32°F to 131°F), no precipitation*:	
— Low Wind Speeds:	4 knots to 10 knots (4.6 MPH to 11.5 MPH)—5° RMS typical
— High Wind Speeds:	>10 knots (>11.5 MPH)—2° RMS typical
Wind Direction Accuracy in wet conditions**:	>8 knots (9.2 MPH)—8° RMS typical
Compass Accuracy:	
—1° static heading accuracy	
—2° dynamic heading accuracy	
Rate-of-Turn:	0° to 70° per second
Rate-of-Turn Accuracy:	1° per second
Rate-of-Turn Data Output Update Rate:	
— 2 Hz—NMEA 0183 (Adjustable up to 10 Hz)	
— Adjustable up to 20 Hz—NMEA 2000	
Pitch and Roll Range/Accuracy:	±50° / <1°
Air Temperature Range:	-25°C to 55°C (-13°F to 131°F)
Air Temperature Resolution:	0.1°C (0.1°F)
Air Temperature Accuracy:	±1°C (±1.8°F)* @ >4 knots (>4.6 MPH) wind
Barometric Pressure Range:	850 mbar to 1150 mbar (25 inHg to 34 inHg, 850 hPa to 1150 hPa)
Barometric Pressure Resolution:	0.1 mbar (0.029 inHg, 0.1 hPa)
Barometric Pressure Accuracy:	±2 mbar (±0.059 inHg, ±2 hPa) when altitude correction is available
GPS Position Accuracy:	3 m (10') with WAAS/EGNOS (95% of the time, SA off)
Operating Temperature Range:	-25°C to 55°C (-13°F to 131°F)
Supply Voltage:	9 VDC to 16 VDC
Supply Current:	<220 mA
Weight:	285 grams (0.7 lb)
Sensor Baud Rate (NMEA 0183 Interface Only):	4,800 bps (can be increased to 38,400 bps with a command)

Table 3. Airmar PB200WX specifications (after Airmar 2011).

2. Existing Datasets of SHARC/Airmar Measurements

Various Wave Glider / SHARC user groups have made measurements in an attempt to evaluate the SHARC Airmar PB200WX. This research is especially important because the Airmar is the standard weather sensor outfitted on the SHARC. Therefore, there exists a potentially vast network of near surface measurements obtained by SHARCs operating over the world's oceans. In particular, LRI examined their Pacific Crossing (PacX) data in comparison to nearby NDBC buoys, Naval Oceanographic Office (NAVO) deployed a SHARC in the vicinity of an NDBC buoy, and NPS co-deployed the SHARC and the MASFlux buoy for weather data collection. These datasets are to be analyzed in this thesis.

a. *LRI PacX Measurements*

In November of 2011, LRI deployed four Wave Gliders from San Francisco, with two heading to Australia and two heading for Japan. This Pacific crossing served as both a test and a demonstration of Wave Glider capabilities. The data collected during this crossing is known as the “PacX” data.

During this deployment, LRI programmed the wave gliders to orbit several NDBC buoys so that they could compare the Airmar / SHARC weather measurements to those reported by the NDBC buoys. On February 18, 2012, the PacX Wave Gliders circled buoy 46012 in Monterey Bay. Similarly, from February 25-27, 2012, three of the PacX Wave Gliders orbited within eight nm of NDBC buoy 51000, located 200nm northeast of Maui. Griffith et al. (2012) focused on the latter dataset for their report on the Wave Glider’s capability as a weather data collection platform.

b. *Datasets by NAVO SHARC Deployments*

NAVO evaluated both the Airmar and the SHARC METOC Plus Model’s GPS wave sensor, the Datawell MOSE Datawell G1000. For the Airmar evaluation portion, NAVO had one SHARC circle NDBC buoy 51002, near Hawaii, from April 7–17, 2012. The SHARC made a hexagon pattern with a 12km radius around the buoy. This area also encompassed one Coupled Ocean/Atmosphere Mesoscale Prediction System (COAMPS) model grid point, and one U.S. Navy coastal ocean model (NCOM) grid point. Figure 10 shows the track of the NAVO SHARC during this evaluation period. NAVO also provided data taken intermittently in Monterey Bay from September 1, 2012–December 5, 2012. Although not collecting data continuously, the SHARCs collected observations in the vicinity of NDBC buoy 46092 for a total of approximately 12 days.

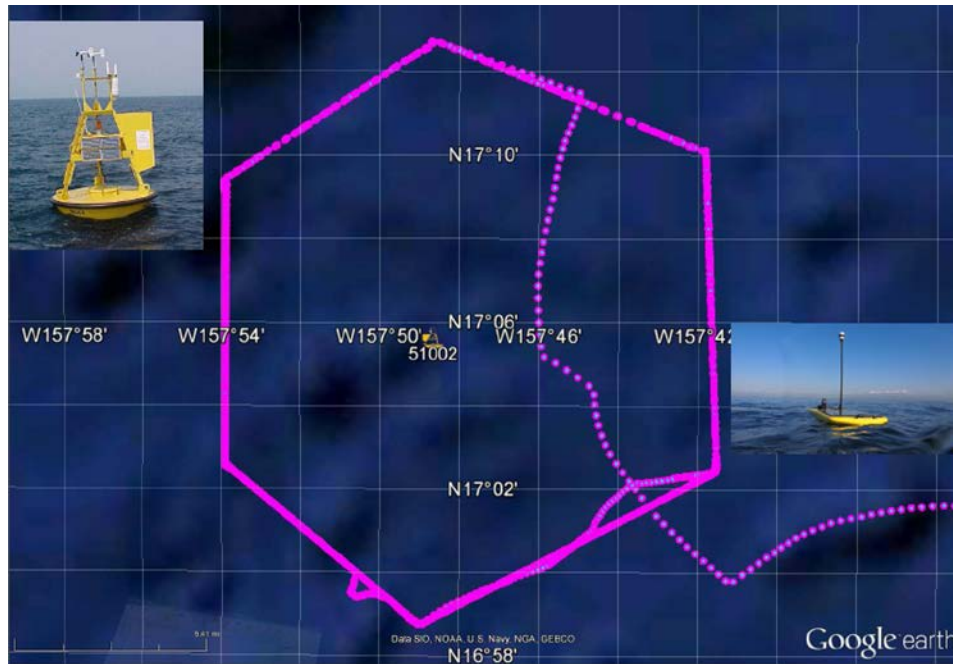
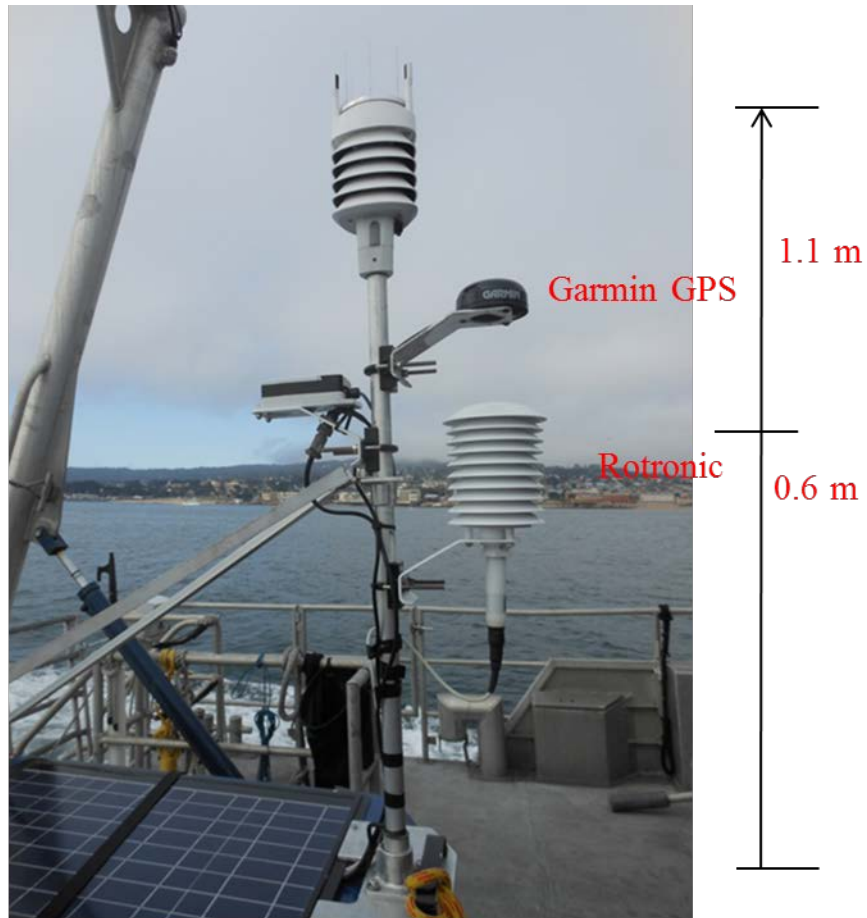


Figure 10. NAVO SHARC track as it orbited NDBC buoy 51002 in April 2012 (from Wang 2012).

III. SHARC INSTRUMENTATION AND TESTING

A. DEVELOPMENT OF CUSTOMIZED METOC PAYLOAD FOR SHARC

The required accuracy of near surface measurements necessitates research grade sensors to be used on a proven platform such as the Wave Glider. Additionally, as described in Chapter II, EDH calculations depend on humidity measurements, which is not available on the default METOC Plus sensor package. The NPS team therefore decided to develop a sensor package for the SHARC with sensors of known quality measurements. This system was mounted on a 1.1 m mast, aft of the SHARC's rear payload bay and measures wind speed and direction, barometric pressure, air temperature, relative humidity, and platform position, velocity, heading, pitch, roll, and six-axis acceleration rates (Figure 11). A separate temperature probe also provides sea surface temperature (SST). Table 4 lists each of the installed sensors and their measured variables. Together, the NPS sensor suite is called the "NPS Met."



Additional
batteries (in
Forward Bay)

Data Acquisition
System (in Aft Bay)

Figure 11. NPS customized METOC sensor suite mounted on the SHARC.

Sensor	Measured variables
Temperature and Humidity Probe Rotronic Model MP100H	Temperature and Relative humidity
Vaisala Weather Transmitter WXT520	Wind speed and direction, Barometric pressure Temperature Relative Humidity
Campbell Scientific Temperature Probe Model 109SS	Sea water temperature
Garmin GPS16-HVS	Position, Velocity, and Magnetic declination
True North Revolution Technologies GS Gyro Stabilized Electronic Compass	Heading, Pitch, and Roll
VectorNav VN-100 Rugged Accelerometer	Angular rates, linear accelerations, and Magnetic field components

Table 4. NPS customized METOC sensor suite and measured variables.

A CR3000 data logger encased in a Pelican model 1400NF case was also installed in the aft payload bay of the SHARC. The dry box was also wrapped in Styrofoam to fit it snugly into the SHARC payload bay (Figure 12). All of the additional instruments described above connected to this data logger as the data acquisition system for the sensor suite. The CR3000 provides approximately 7.5 hours of data collection.

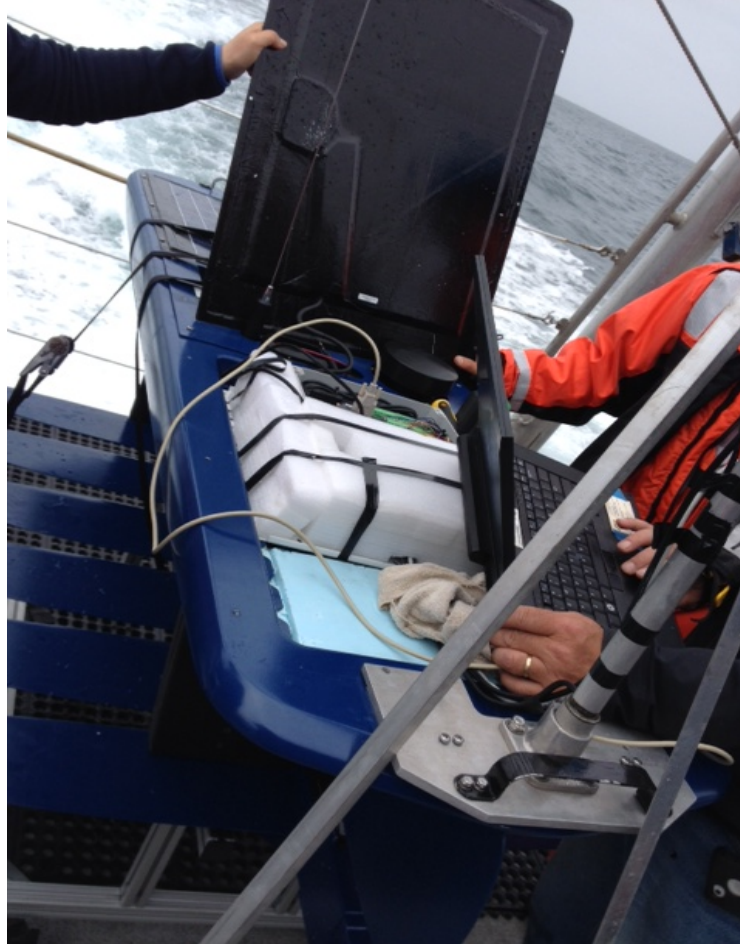


Figure 12. Open aft payload bay, with dry box and data logger shown.

The new sensor payload on the SHARC serves two purposes during the NPS SHARC deployments in 2014. First, the new sensor suite mirrors the sensors used on the NPS MASFlux buoy, a system that had been previously tested and proven (Zuniga 2013). Co-deployment of the SHARC and the MASFlux buoy facilitates a direct comparison of the datasets collected by the two platforms. This comparison ensures we are able to accurately measure the mean near-surface properties of the atmosphere from the SHARC. Secondly, it provides co-located measurements for thorough evaluation of the Airmar PB200WX with known quality sensors. This configuration allows for a more robust evaluation of the Airmar PB200WX in comparison with data from a nearby buoy in previous study.

B. NPS SHARC SENSORS

The following paragraphs describe the uses and design of the sensors NPS installed on the SHARC. Table 5 lists manufacturer stated accuracy and ranges of the METOC sensors, GPS, accelerometer, and compass.

NPS Sensor and Instrument Specifications				
Temperature and Humidity Proberotronic Model MP100H				
Parameter	Temperature	Humidity		
Range	-40 to 60 (C)	0 to 100 (%RH)		
Accuracy	0.03 (K) (Pt100) 0.3 (K) (HygroClip)	1.5 (%RH)		
Vaisala Weather Transmitter WTX520				
Parameter	Pressure	Wind Speed	Wind Direction	
Range	600 to 1100 (hPa)	0 to 60 (ms ⁻¹)	0 to 360 (deg)	
Accuracy	0.5 (hPa) 0 to 30 C 1 (hPa) -52 to 0, 30 to 60 C	3% at 10 ms ⁻¹	3 (deg)	
Resolution	0.1 (hPa)	.1(ms ⁻¹)	1 (deg)	
Campbell Scientific Temperature Probe Model 109SS				
Parameter	Temperature			
Range	-40 to +70 (C)			
Accuracy	.49 at -20 to +70 (C)			
Response time	36 (msec)			
Dip angle	+/- 80 (deg)			
Tilt range	+/- 40 (deg)			
Garmin GPS 16-HVS				
Parameter	Position	Velocity		
Range	+/- 40 (deg)	+/- 40 (deg)		
Accuracy	3 m	0.1 RMS (steady state)		
PPS Rate	+/- 1 (μs)	+/- 1 (μs)		
Repeatability	+/- 0.2 (deg)	+/- 0.2 (deg)		
VectorNav VN-100 Rugged Accelerometer				
Parameter	Attitude	Heading	Acceleration	Magnetic Field
Range	+/- 90 (deg)	+/- 180 (deg)	+/- 8 (g)	+/- 2.5 (Gauss)
Accuracy	0.5 (deg)	2.0 (deg)	+/- 0.05 (deg)	+/- 0.05 (deg)
Resolution	0.05 (deg)			
Linearity			0.5% (FS)	0.1% (FS)

Table 5. Manufacturer stated accuracy and ranges of the NPS customizer METOC sensors, GPS, accelerometer, and compass package.

1. Rotronic Model MP100H Temperature/Humidity Probe

This instrument includes two sensors to measure relative humidity and temperature. The HygroClip S3 samples relative humidity while the Pt100 samples air

temperature. According to Zuniga (2013) the instrument is less prone to errors typically caused by solar radiation and precipitation. Data were collected at 1Hz.

2. Vaisala Weather Transmitter WXT520

The WXT520 measures and calculates two-dimensional wind speed and direction, and barometric pressure. The sensor uses three transducers and ultrasound technology to determine horizontal wind speed and direction. Importantly, this open sensor design does not impede wind flow at large angles of platform pitch and roll as compared to the Airmar sonic system (Lind 2014, personal communication). Data were collected at 1Hz.

3. Campbell Scientific Temperature Probe 109SS

A CS 109SS was installed in the aft payload bay and extends through a small hole in the underside of the SHARC hull to measure SST. The probe extends approximately 1 inch from the hull into the water. On the third day of field testing, three small Onset recording thermometers were affixed to the hull to provide additional SST data for comparison.

4. Garmin GPS 16-HVS

This GPS tracks platform speed and direction, largely used to calculate true winds. The GPS can track up to 12 satellites and receives one second navigation updates. Additionally, the 16-HVS model is waterproof, which makes it well-suited for maritime use.

5. True North Revolution Technologies GS Compass

The GS model compass is specifically designed for platforms operating in dynamic environments such as rough seas. The GS uses a 3-axis solid state magnetometer to provide accurate heading, pitch, and roll data. Zuniga (2013) reported reduced uncertainty in MASFlux heading data after adding the GS compass.

6. VectorNav VN-100 Rugged Accelerometer

The VN-100 Rugged is an inertial measurement unit (IMU) and Attitude Heading Reference System (AHRS). The VN-100 combines three-axis accelerometers, three-axis gyros, and 3-axis magnetic sensors to provide three-dimensional platform orientation data. According to Zuniga (2013), there is uncertainty in the yaw measurements. Data were collected at a rate of 5Hz.

C. FIELD TESTS OF NPS SHARC INSTRUMENTATION

The NPS Meteorology Department sought to further evaluate the Airmar in expanded conditions and in a controlled environment. We conducted static intercomparisons and at-sea testing in Monterey Bay. More details are available in the below sections.

1. Static Intercomparison

The NPS Meteorology Department conducted a comparison of the Airmar and the new instrument package in a controlled environment. Both the Airmar and the new sensor package were removed from the SHARC and mounted on a frame as shown in Figure 13. The team collected data on the roof of a six story building from September 18 to October 6, 2014. The two masts were then moved to an open area on Fort Ord in Marina, CA from October 6–24, 2014 in order to expose the sensors to higher wind conditions. From November 26 through December 6, 2014, the static test resumed atop the six story building to confirm some of the initial data. These static datasets allow for direct comparison of the 1Hz data from the new NPS sensors, with the raw 1Hz data from the Airmar (as opposed to the 10-minute averaged data integrated into the LRI data management system). Additionally, the static test removes the platform motion from the problem.

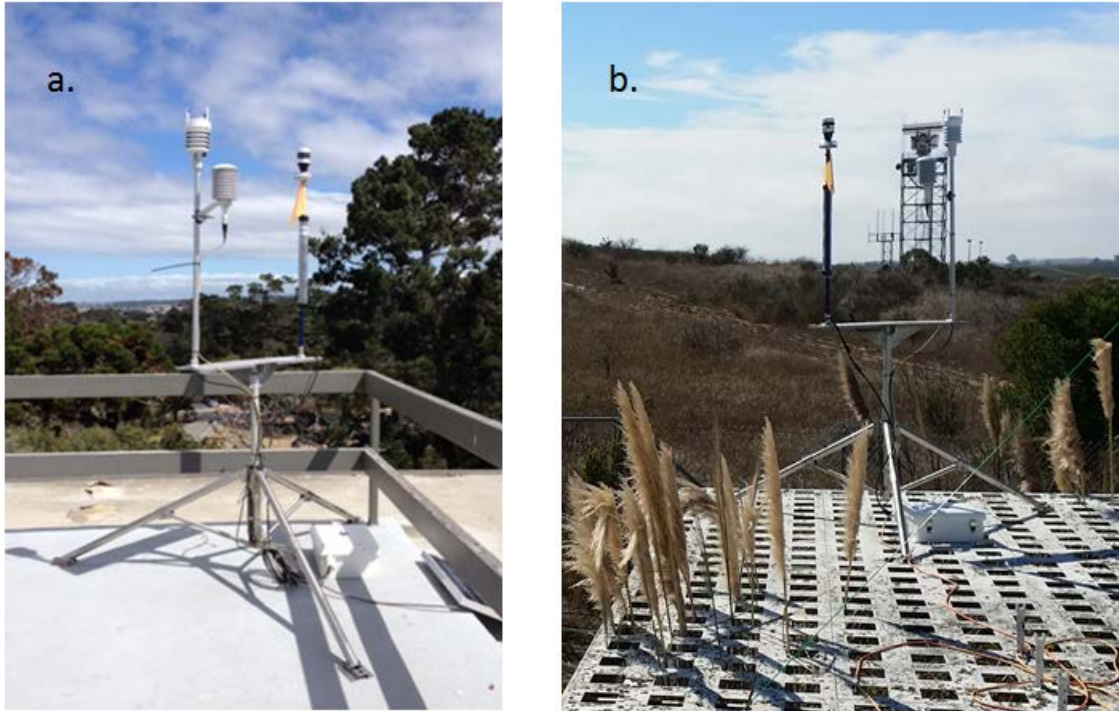


Figure 13. Static testing of the Airmar PB200WX and the NPS sensor package a) atop a six floor building and b) at Fort Ord, Marina, CA.

2. At-Sea Testing

NPS conducted three field tests of the SHARC in Monterey Bay on July 29, July 30, and August 8, 2014, respectively. Not only did the SHARC host the new sensor package as described above, the SHARC was also co-deployed with the NPS MASFlux buoy. The SHARC received frequent steering updates to keep it within 2km of the MASFlux buoy throughout the five hours of data collection each day.

a. MASFlux Configuration

The MASFlux buoy, with its near surface measurements and small size, is most suitable for evaluating the SHARC meteorological and upper ocean measurements. The MASFlux buoy features well calibrated wind, temperature, and humidity sensors at multiple levels within the lowest 4 m of the surface, concurrent wave and upper ocean temperature measurements, and turbulent flux measurements using direct eddy correlation method, which is the ‘golden standard’ flux measurement compared to bulk

methods. As described above, the MASFlux buoy consists of the same sensors as the SHARC: the Rotronic humidity and temperature probe, Vaisala weather transmitter WXT520, Campbell Scientific temperature probe 109SS, Garmin GOS16-HVS, True North GS Electronic Compass, and VectorNav VN-100 Rugged accelerometer. With its similar configuration and known quality, the MASFlux data can be used to examine the feasibility of using the current METOC glider measurements in quantifying various properties at the air-sea interface from wave glider measurements, and for further use in surface flux parameterizations and forecast models.

Additionally, the MASFlux buoy hosts the Ultrasonic Anemometer R M Young Model 81000VRE. This sensor provides critical measurements for obtaining turbulent flux calculations. In particular, this instrument measures three-dimensional wind velocity, and the speed of sound at a rate of 20 Hz. For details of the MASFlux instrumentation, refer to Zuniga (2013).

Figure 14 shows the MASFlux buoy and SHARC tracks from each day. Different weather conditions were encountered on the three days of field testing and different techniques for co-deploying the SHARC and MASFlux were tested. On both July 29 and 30, 2014, winds and seas were calm. On August 8, 2014, winds again were calm but there were 1.5m swells and confused waves. Table 6 shows the weather conditions for each day as reported by nearby NDBC buoys.

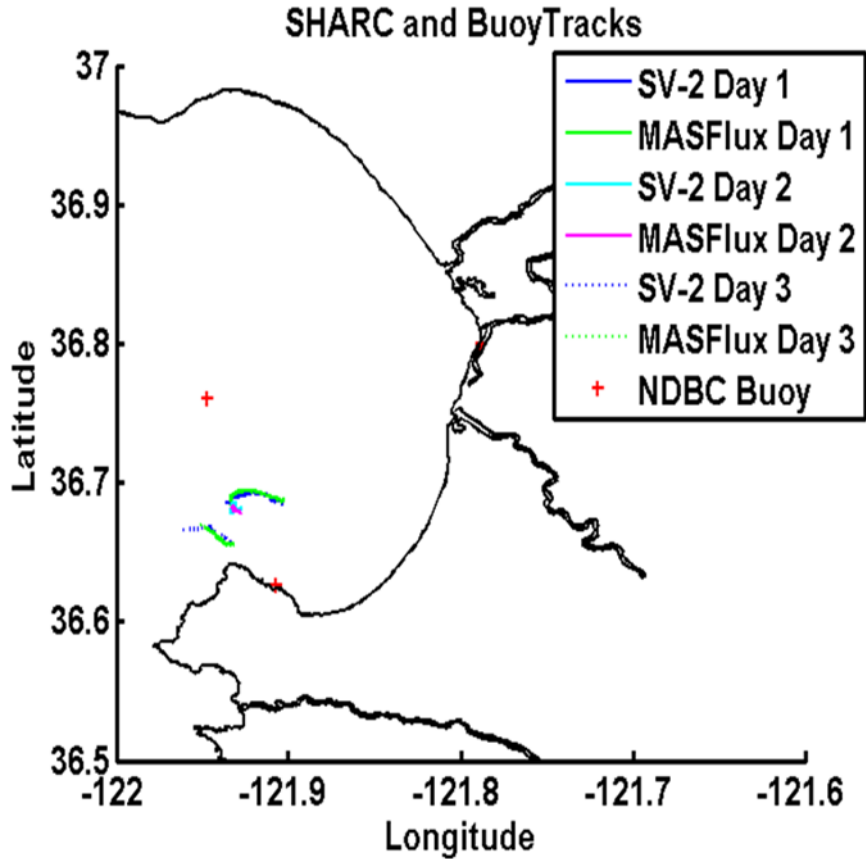


Figure 14. SHARC and MASFlux tracks during at-sea field testing.

NDBC Buoy 46236 (Monterey Canyon Outer)	29-Jul-14	30-Jul-14	8-Aug-14
Wave Height (m)	0.86	1.02	1.61
Dominant Wave Period (s)	8.33	8.33	8.33
Avg Wave Period (s)	6.49	5.77	6.64
SST (C)	17.8	17.7	17.4
NDBC Buoy 46092 (MBARI)			
Wind Speed (m/s)	3	5	7

Table 6. One hour averages as reported by NDBC buoys at 1102 PDT on each deployment day.

The sensors performed well each day with a few exceptions. On July 30, R/V *Fulmar* remained too close to the MASFlux buoy while the buoy was deployed. Frequent

backing down of the Fulmar created ocean mixing and possibly flow disturbance. The situation was corrected for future testing days by having the research vessel maintain at least .5 km separation from the SHARC and MASFlux buoy during data collection. Additionally, extra temperature probes were added to the SHARC for the August 8 deployment to gather more data for comparison.

b. Deployment and Recovery Procedures

All deployments and recoveries were conducted from the stern of the (R/V) *Fulmar*, a 66'9" catamaran. The Fulmar features a 2000lb A-frame that the crew used for hoisting the SHARC into and out of the water. These evolutions are dynamic and challenging, and the NPS team's proficiency in deploying, recovering, and operating the SHARC increased on each deployment day.

In particular, deployment and recovery procedures of the wave glider were improved and codified over the three underway days. For SHARC recovery, the NPS crew must communicate with the R/V *Fulmar* captain to intercept the SHARC by maneuvering the *Fulmar* so that the *Fulmar's* fantail is on the glider's starboard side. Then, it is critical that the captain place the Fulmar in neutral to avoid backing over the SHARC. Attaching fore and aft taglines to SHARC before deployment (and leaving them attached throughout that day's underway) also greatly improves both the deployment and recovery processes. Not only were the tag lines used to stabilize the SHARC while being lifted by the A-frame, but the tag lines also allowed the Fulmar to stay farther away from the SHARC during recovery. Finally, during data collection, the Fulmar must maintain at least 1000m separation from both the SHARC and the MASFlux buoy to prevent the *Fulmar* from disturbing the flow characteristics and environmental conditions being measured.

THIS PAGE INTENTIONALLY LEFT BLANK

IV. NPS MET SENSOR PERFORMANCE AND AIRMAR EVALUATION

The NPS team evaluated the new NPS Met package and the standard SHARC weather sensor, the Airmar PB200, against known, high-quality environmental measurements. First, the team compared the NPS Met data to that collected from the MASFlux buoy. Not only did this step allow the team to determine the quality of the NPS Met suite, but it also allowed the team to determine whether the SHARC platform adds distortion to the near surface measurements collected from the SHARC. This evaluation aims to determine the suitability of both the SHARC platform and the NPS Met suitability for air-sea data collection. Additionally, after validating the NPS Met instruments, they can provide a set of known, quality measurements against which to compare the Airmar data. The Airmar data collected by NPS then are compared to the NPS Met data, and the Airmar measurements provided by NAVO and LRI are compared to NDBC Buoy 46092 in Monterey Bay.

A. NPS MET PAYLOAD EVALUATION

As described in Chapter II, the NPS Met sensors mirror those used on the MASFlux buoy. The following sections show the comparison between the NPS Met and MASFlux wind, specific humidity, pressure, and temperature measurements collected at sea. In general, a separate time series was plotted for each variable, and for each day of at sea testing. The scatter plot uses the combined data from all three days of underway testing. The red line on the scatter plot represents a one-to-one relationship between the two data sets. Perfectly correlated and unbiased data would fall on that line. Both the time series and scatter plot graphs show a 10 minute moving average of the data. This moving average permits more direct comparison of the mean values from the different sensor packages or platforms and smooths the datasets.

1. Wind Speed and Direction Measurements

Wind speed measurements for each testing day show wind speed generally increasing with height, which is consistent with MOST (Figure 15). On each day of

testing, the winds gradually increased over time but remained light. On the SHARC, the NPS Met sampled wind speed at a height of 1.1 m. This height falls between the MASFlux wind speed sensor levels one and two. Therefore, we expect the NPS Met wind speed to fall between the MASFlux levels one and two wind speeds. Graphically, this means the magenta line (NPS Met) should be in between the green and red lines (MASFlux levels one and two, respectively). With minor exception, this trend does hold true on all three days.

Figure 16 shows the strong correlation between the NPS Met wind speed data and the MASFlux level one on all three days. The small positive bias of the NPS Met is due to the fact that the NPS Met wind speed sensor is mounted higher than the level one MASFlux buoy wind sensor. Also, although the MASFlux buoy and the SHARC were within 1.5 km of each other during all at-sea testing, they were not exactly collocated. This small spatial variability also accounts for small differences between the two platforms' measurements.

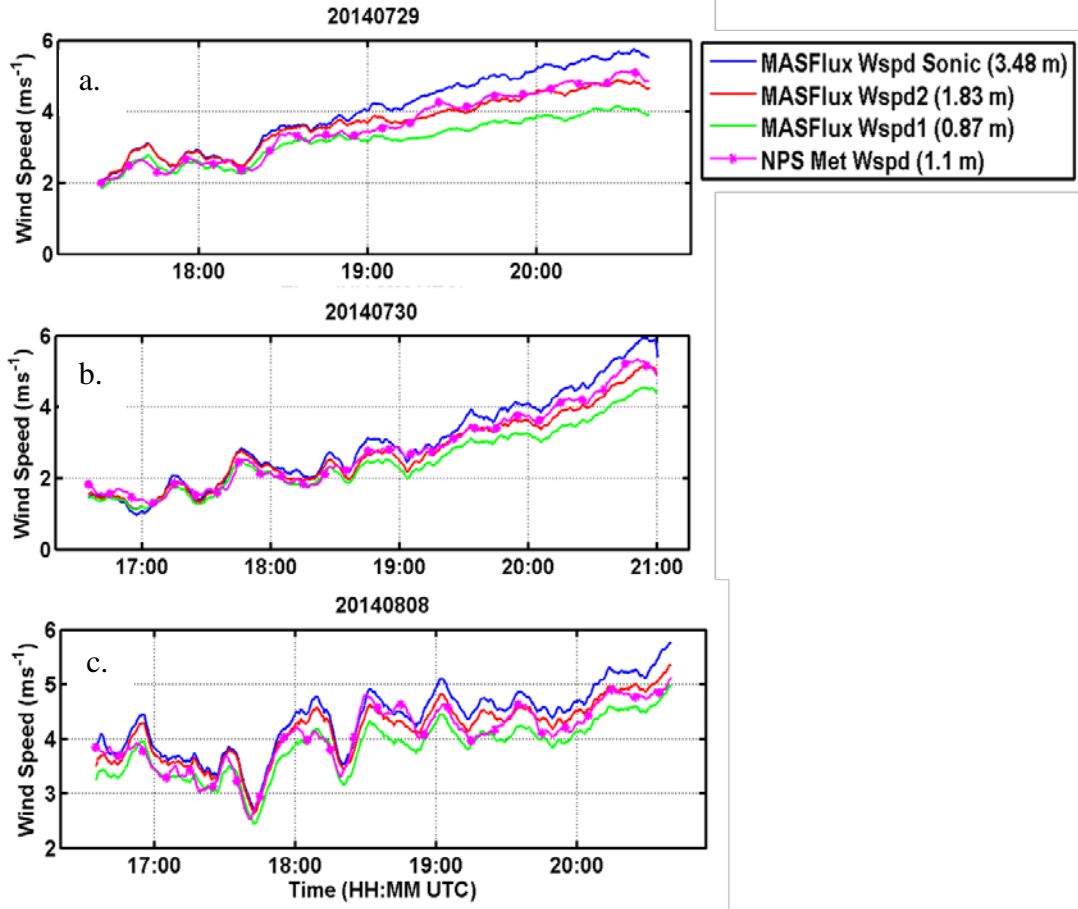


Figure 15. Time variation of the MASFlux and NPS Met wind speed measurement on a) July 29, 2014; b) July 30, 2014; c) August 8, 2014.

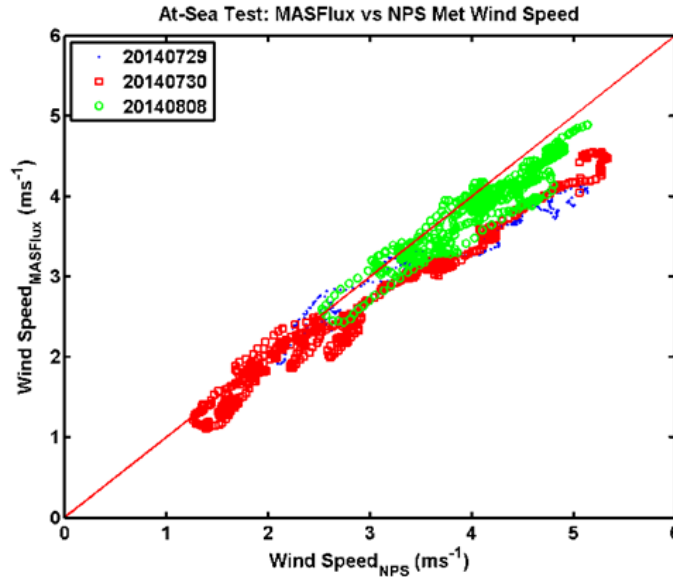


Figure 16. Comparison of the level one MASFlux wind speed measurements and the NPS Met wind speed measurements during at sea testing.

Comparisons of the wind direction during at-sea testing are shown in Figure 17. Winds remained Southwest to Northwest on all three days and should not vary over the 4 m height of the NPS Met and MASFlux sensors. Therefore, the wind direction measurements should be identical from all of the MASFlux wind sensors. In general, the NPS Met wind direction measurements follow the same trend as the MASFlux measurements but with some variation. The scatter plot shows generally good correlation (Figure 18) between NPS Met and MASFlux level one wind direction measurements. Wind direction measurements from July 30, 2014 show slightly decreased correlation compared to the other two days of at-sea testing. Again, spatial variation accounts for some differences in the two datasets. Additionally, removing the movement of the SHARC platform from the NPS Met observed winds was more challenging when the SHARC made a lot of turns. On day two of testing (July 30, 2014), the NPS team steered the SHARC in a tighter pattern to stay within 0.5-1.0 km of the MASFlux buoy. This tight pattern, increased SHARC turning, and more difficult data processing may account for differences in the wind direction, as well.

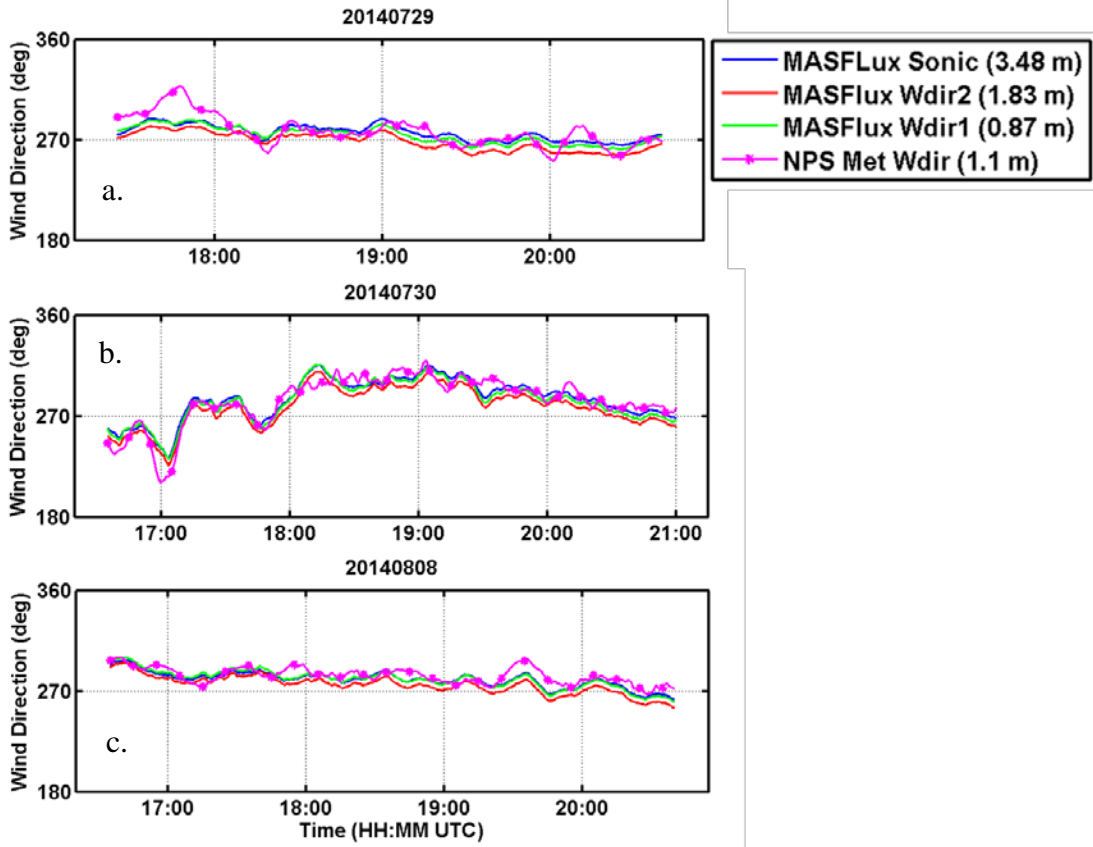


Figure 17. Same as Figure 15, except for wind direction.

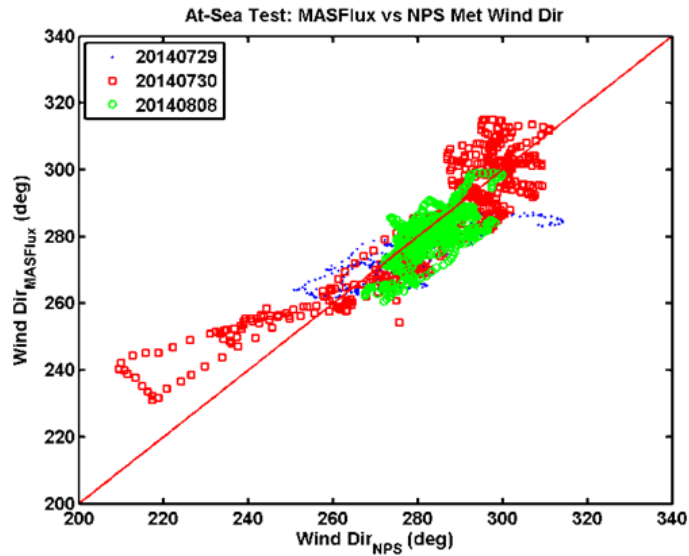


Figure 18. Same as Figure 16, except for wind direction.

2. Specific Humidity

Figure 19 shows the time series plots of the at-sea specific humidity that was calculated using the relative humidity measurements from the NPS Met and MASFlux sensors. On July 29 and July 30, 2104, the level one MASFlux RH sensor went underwater during deployment and was inoperable for the remainder of those two days. Therefore, only MASFlux levels two through four are shown for July 29 and 30, 2014. Due to surface evaporation, RH and specific humidity decrease sharply with height as seen in the lowest ~20 m of the atmosphere. The NPS Met samples relative humidity at a height of 0.6 m and should have specific humidity values greater than those measured by the MASFlux level two, and less than those values measured by level one of the MASFlux, when available. This trend is observed on all three days of testing. Figure 20 shows very strong correlation between NPS Met and the level two MASFlux specific humidity. The small bias, approximately 0.15 gKg^{-1} , is likely caused by the vertical gradient and spatial variability.

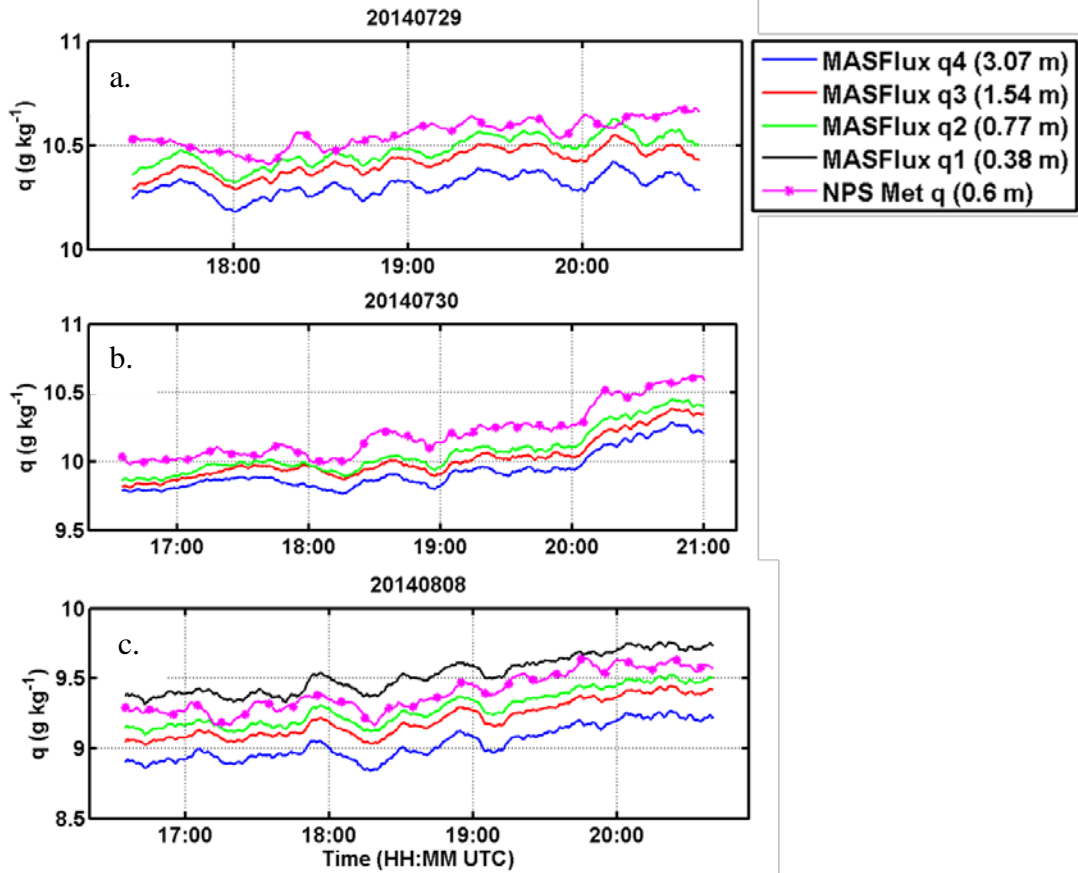


Figure 19. Same as Figure 15, except for specific humidity.

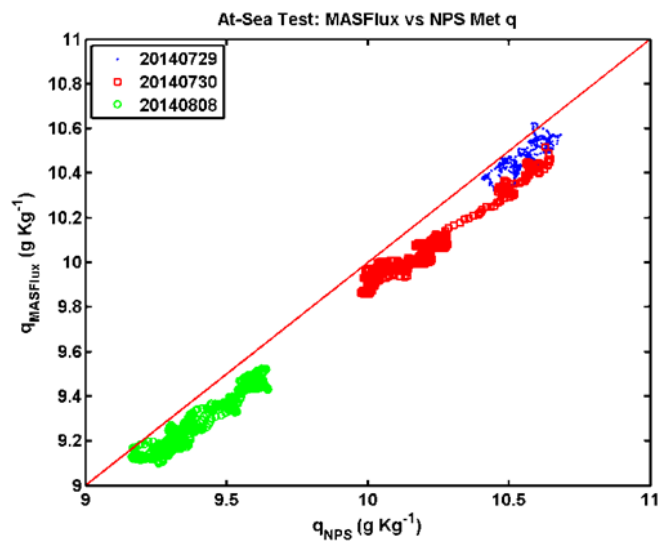


Figure 20. Same as Figure 16, except for specific humidity.

3. Pressure

Figure 21 is the time series plots of the at-sea NPS Met and MASFlux pressure measurements and Figure 22 shows the scatter plot for all three days. There is nearly perfect correlation between the two platforms and their respective instruments. The NPS Met pressure sensor has a bias of -0.14 mb which is within the accuracy limits of the two sensors. Therefore, the pressure measurements from the NPS Met and the MASFlux buoy are statistically identical.

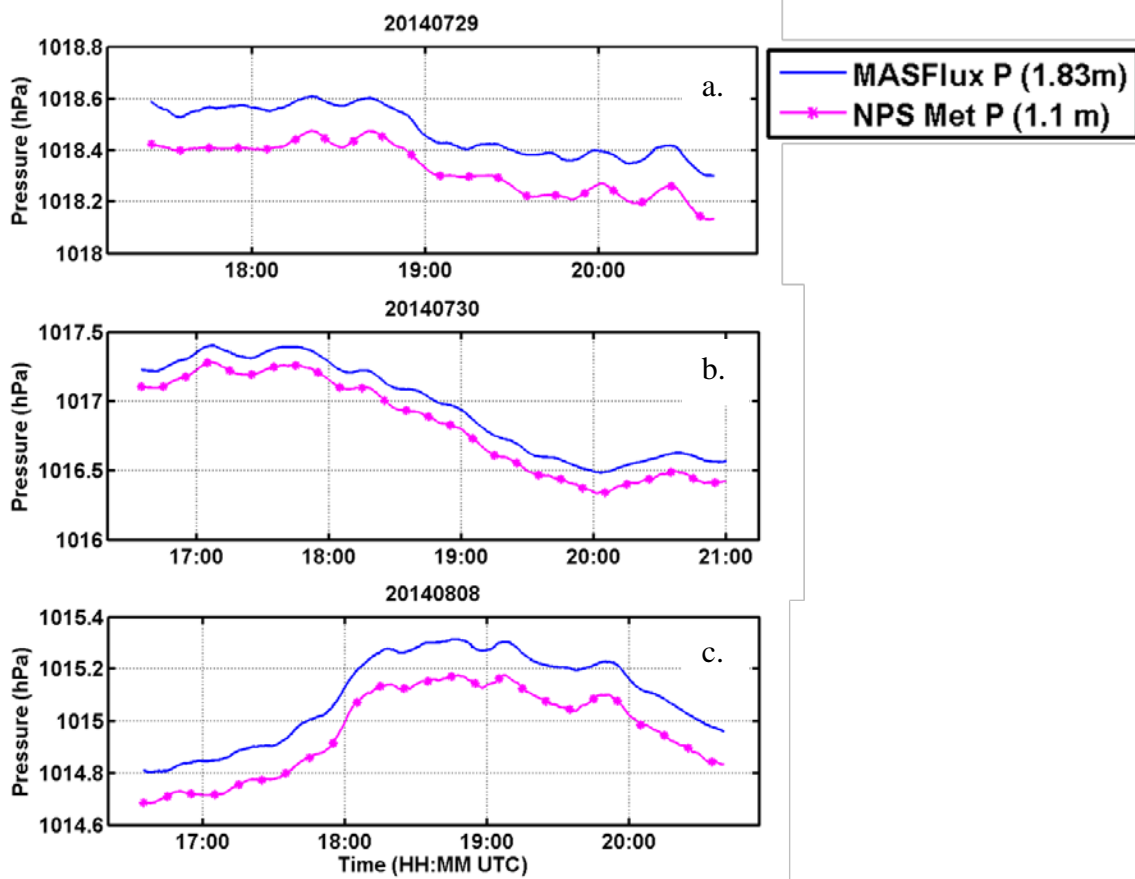


Figure 21. Same as Figure 15, except for pressure.

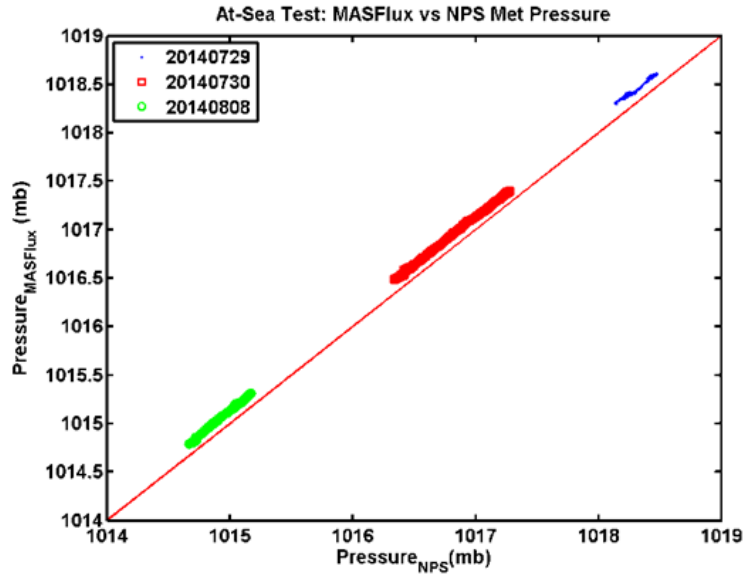


Figure 22. Same as Figure 16, except for pressure.

4. Temperature

Figure 23 shows the SST and air temperature measurements from the NPS Met and MASFlux sensors. On each of the three at-sea days, SST was warmer than air temperature, denoting unstable thermal stratifications. The air temperature decreased with height and SST decreased with increasing depth, as expected. The NPS Met SST, in general, does not show as much variability as the MASFlux measured SST. On July 30, 2014, the R/V *Fulmar* stayed within approximately .25 km of the MASFlux buoy and periodically backed down to maintain position. This action caused a lot of mixing in the area of the MASFlux buoy, brought cooler water to the ocean surface, and introduced additional variability in the sampled SST. On August 8, 2014, there was high swell so a greater distance between the SHARC and MASFlux buoy had to be used. The sharp gradient in SST visible on that day may be an ocean front and the distance between the two platforms could explain why the two platforms encountered the front at different times.

For air temperature, the NPS Met samples the air at 0.6 m which is between the MASFlux levels one and two. On Jul 29 and July 30, 2014, the MASFlux level one temperature sensor malfunctioned for the same reason described above in section 2.

Therefore, only MASFlux levels two through four are shown for those days. Since air temperature decreases with height in the observed unstable condition, the NPS Met air temperature should be greater than those measured by the MASFlux level two, and less than those values measured by level one of the MASFlux, when available. This trend is observed on all three days of testing with a few deviations likely caused by the spatial variability described above. Figure 24 shows strong correlation and an absolute error of only 0.05 degrees Celsius between the NPS Met air temperature measurements and the MASFlux level two air temperature measurements.

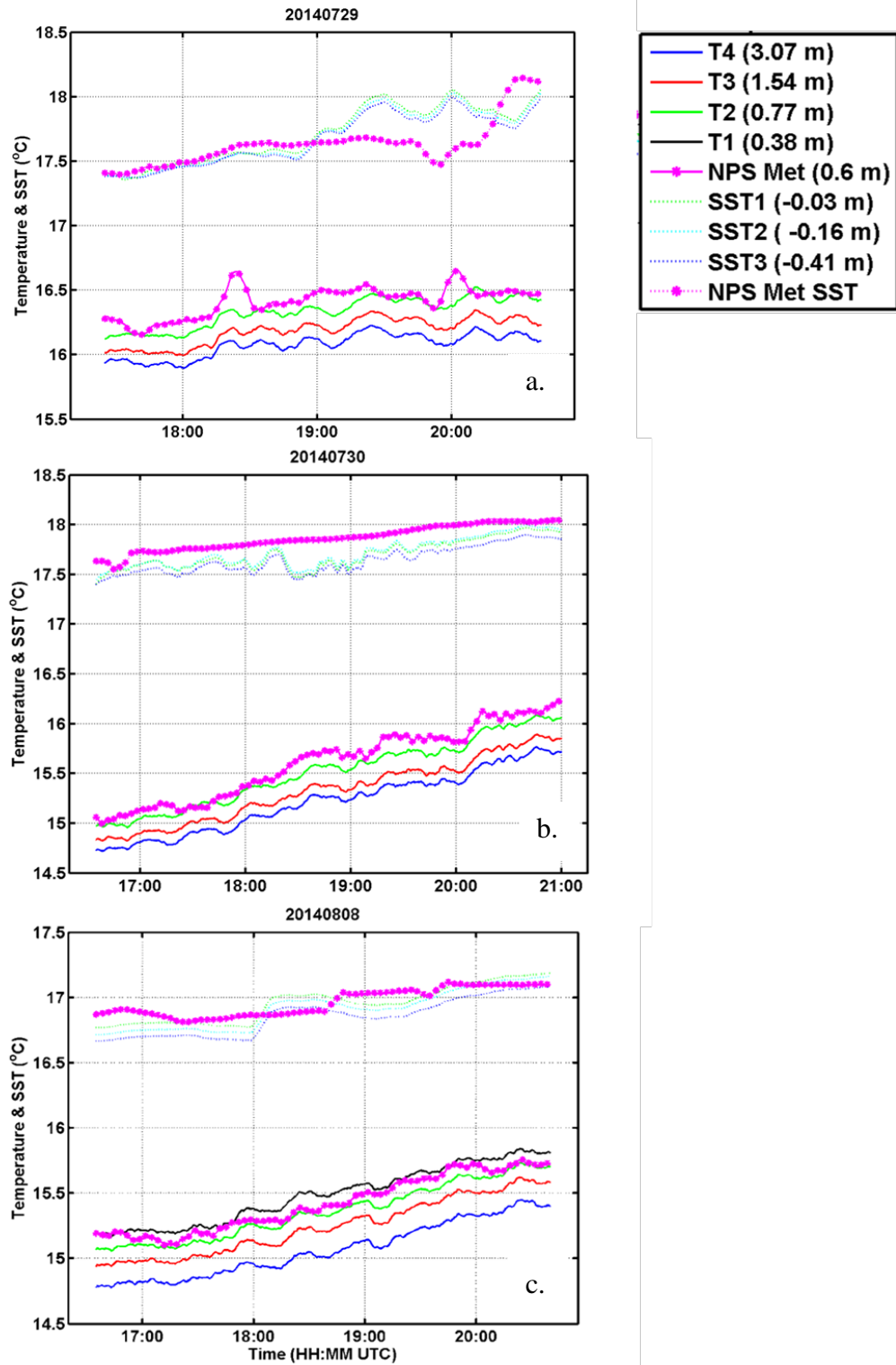


Figure 23. Same as Figure 15, except for temperature.

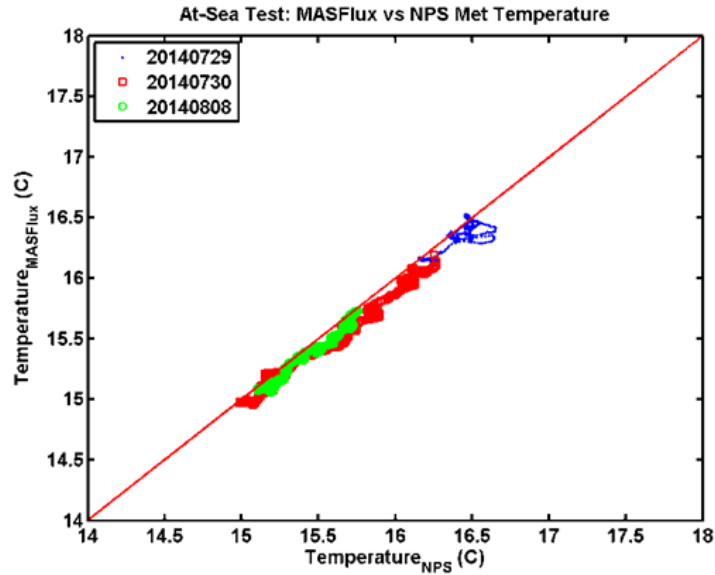


Figure 24. Same as Figure 16, except for air temperature.

5. Solar Heating Effect

The data above show that the effect of the platform on air temperature is minimal and sampling error from the NPS Met is likely from other sources. Solar heating of the instrument housing is known to affect the accuracy of all naturally ventilated air temperature sensors, such as the Rotronic model used on both the MASFlux and NPS Met. As stated in Chapter II, air-sea fluxes and near surface gradient calculations require high quality, accurate mean measurements. Therefore, while this solar heating will not be apparent in the NPS Met and MASFlux comparison testing, it is still important to consider this effect when attempting to determine temperature accurately.

An R. M. Young radiation shield was used with the Rotronic MP100 to reduce solar heating of the sensor. Even with the housing shield, however, the radiation heating effect may still be sizeable in some conditions such as low winds and clear skies. Figure 25 shows the relationship between solar heating, the natural ventilation rate, and the sun angle. In general, one would expect to see a significant solar heating effect in low wind conditions and when the sun is lower in sky. Of note, the Airmar does not have an effective radiation shield and is therefore likely more susceptible to heating from

incoming irradiation than the NPS Met instrument. This point will be discussed in a later section.

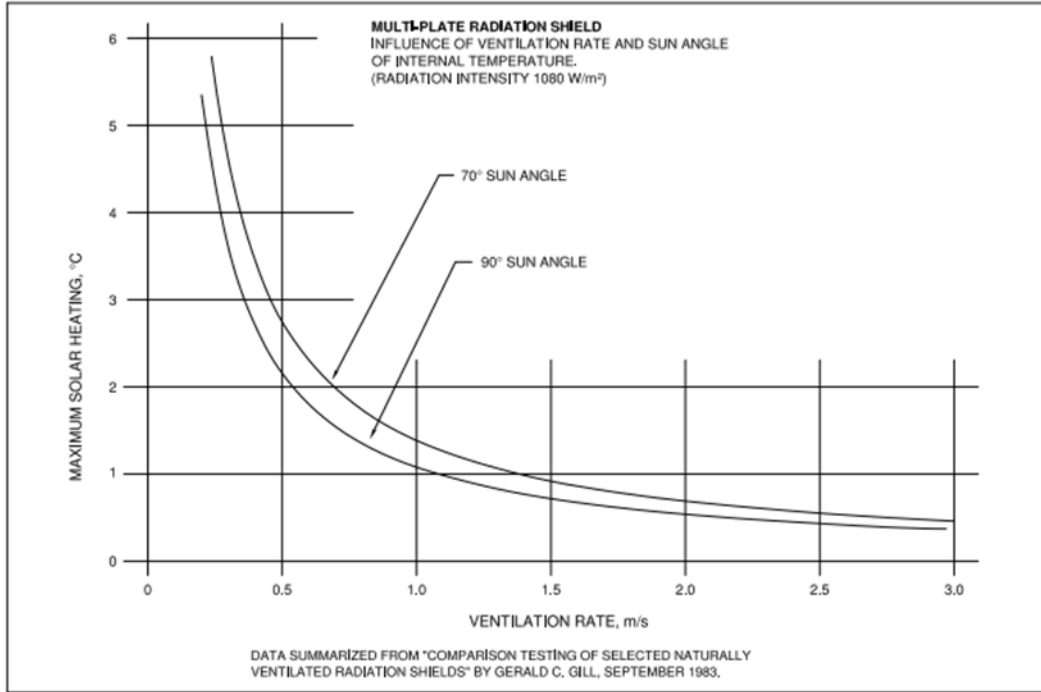


Figure 25. Relationship of the solar heating of the multi-plate radiation shield used on the Rotronic sensor to the ventilation rate and sun angle (from R. M. Young, 2012.)

In order to identify the signature of solar heating in the temperature data, the NPS Met and a solar irradiance sensor collected data simultaneously at Fort Ord. Figure 26 shows the data collected on October 9 and October 10, 2014. October 9, 2014 is a typical sunny day as evident by the high peak value of solar irradiance and smooth irradiance curve. Figure 27 shows the data collected on October 17 and October 18, 2014 and represents a typical cloudy day as evident by the lower peak solar irradiance value and a “fuzzy” irradiance curve. On the sunny day, there are two peaks in NPS Met air temperature which correspond to the period of steep changes in solar irradiance. It is also possible that some direct sunlight was reaching the NPS temperature sensor at lower sun

angles. On the cloudy days, in contrast, there are no extra peaks in the NPS Met temperature data due to the light being more diffuse.

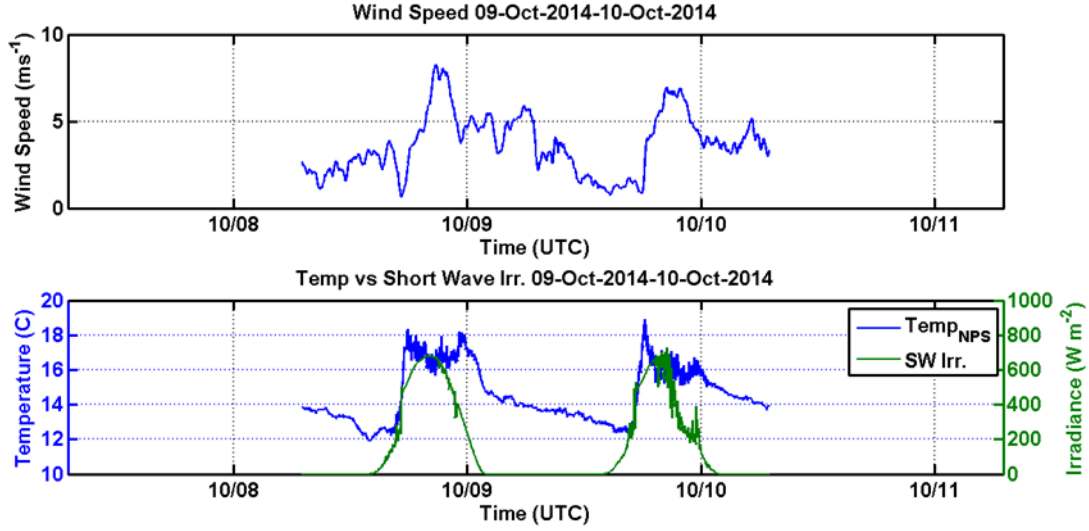


Figure 26. Typical measurements of NPS Met temperature, incoming solar irradiance, and wind speed at Fort Ord during the intercomparison testing on a sunny day.

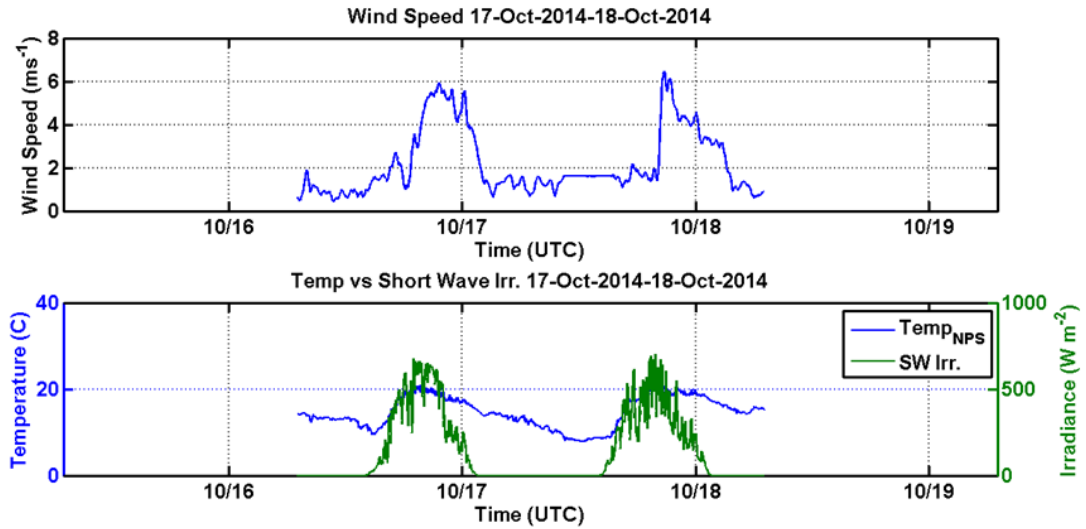


Figure 27. Same as Figure 26, except for a cloudy day.

6. NPS Met Mean Measurement Conclusions

Overall, the NPS Met and MASFlux mean measurements are highly correlated and display only small biases due to spatial and temporal variability. Table 7 summarizes the statistical comparison between the NPS Met and MASFlux buoy data. The SHARC platform does not introduce significant flow distortion for the mean measurements in comparison with the small and drifting MASFlux buoy. Therefore, the NPS team feels confident of the NPS Met payload system and will use it as the “truth” for evaluating Airmar data.

MASFlux (Levels Indicated) vs NPS Instruments At Sea (Moving 10 Minute Averages)				
	Press (mb)	Temp L2 (C)	Wind Sp L1 (ms ⁻¹)	RH (%)
Mean Error	0.14	-0.08	-0.31	0.52
Error Std Dev	0.01	0.06	0.29	0.32
Abs Error	0.14	0.08	0.33	0.55
Corr Coef	1.00	0.99	0.97	0.99

Table 7. Statistical comparison of MASFlux and NPS Met measurements during at sea testings.

B. NPS TESTING AND EVALUATION OF THE AIRMAR

The NPS team conducted both at-sea, and land-based static testing of the Airmar PB200 weather station. Analysis of these data and their comparison with the NPS Met data collected concurrently is detailed below.

1. NPS Airmar at Sea Testing

The SHARC transmits 10 minute averaged Airmar weather data. To evaluate the at-sea data, I averaged 10 minutes of NPS Met data for direct comparison with the Airmar data from the SHARC. The Airmar and NPS Met were separated by only 0.5 m on the SHARC which virtually eliminates spatial and temporal variability between the two datasets. Therefore, if both instruments are providing high quality measurements, the data should be statistically identical.

Figure 28 is the time series plots of the averaged Airmar and NPS Met pressure data collected during the three days of at-sea testing. While the Airmar captured the

overall pressure trend each day, it did not handle the details well. The Airmar tended to underestimate the pressure and introduced a large amount of variability not present in the NPS Met data. Figure 29 shows the low correlation between the Airmar and NPS Met pressure.

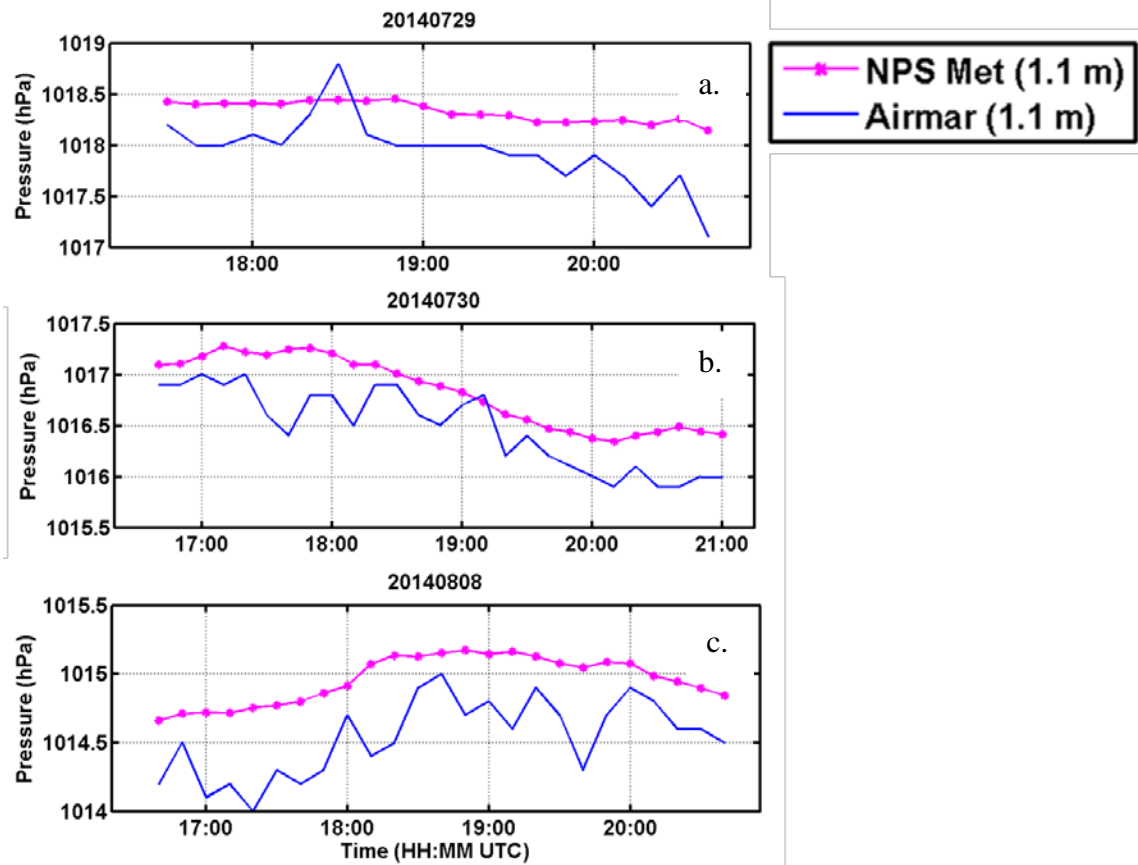


Figure 28. Time variation of Airmar and NPS Met pressure measurements during at sea testing on a) July 29, 2014; b) July 30, 2014; c) August 8, 2014.

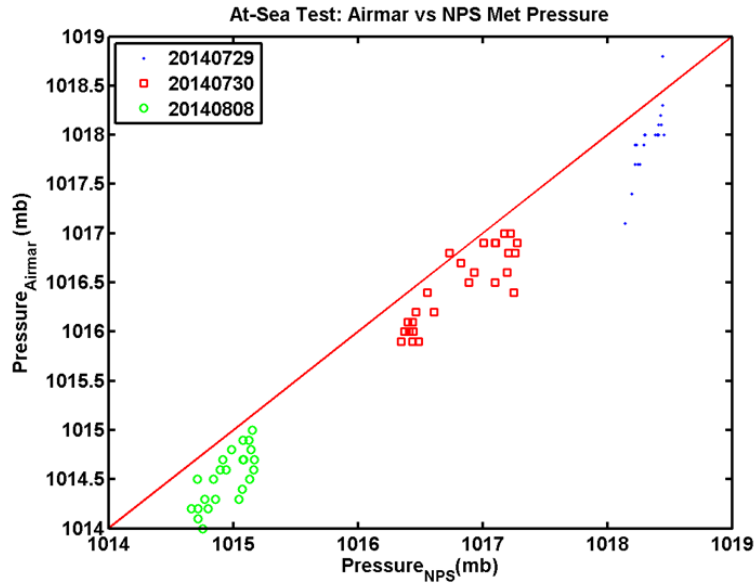


Figure 29. Comparison of the Airmar pressure measurements versus the NPS Met pressure measurements during at-sea testing.

The Airmar performed better with measuring wind speed and wind direction at sea, as shown in Figure 30. The data are not statistically identical but they are well-correlated as shown in Figure 31.

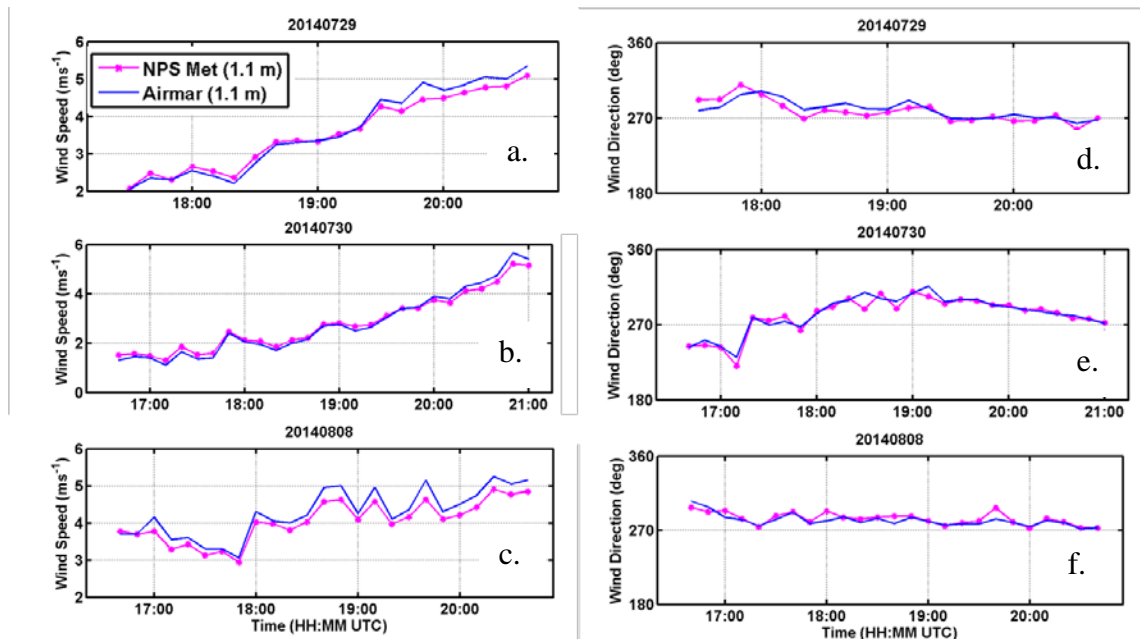


Figure 30. Time variation of Airmar and NPS Met wind speed measurements

during at sea testing on a) July 29, 2014; b) July 30, 2014; and c) August 8, 2014; and time series plots of wind direction measurements on d) July 29, 2014 e) July 30, 2014 and f) August 8, 2014.

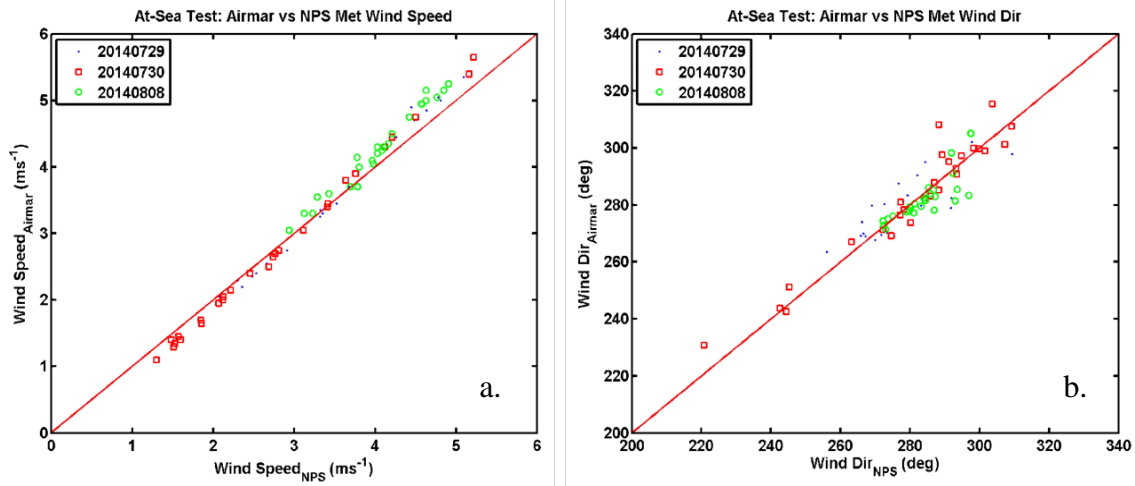


Figure 31. Same as Figure 29, except for a) wind speed; b) wind direction.

2. NPS Airmar Static Testing

The NPS team made static intercomparison using the Airmar and NPS Met in order to evaluate the Airmar’s raw 1 Hz data. Figure 32 shows the time variation of the raw data for each of the measured variables. Red indicates Airmar measurements while blue indicates NPS Met measurements. Just as with the at-sea data, the Airmar captures the pressure and temperature trends but not the details, and introduces additional variability. The Airmar performs well particularly with wind measurements.

Of note, the Airmar overestimated the pressure during the static test, whereas it underestimated the pressure during the at-sea testing. The 10 minute averages of the static test data from the SHARC data management computer also remained higher than the NPS Met measurements, indicating no additional calibration of the Airmar original data by the LRI data system. The bias of about 5 mb in pressure seems to be consistent with previous studies of LRI (Griffith et al. 2012) and Naval Research Laboratory (Wang and Allard, 2012) although the latter were both from measurements at sea. The negative bias from NPS at-sea testing is thus puzzling and requires more at-sea testing to fully address and quantify.

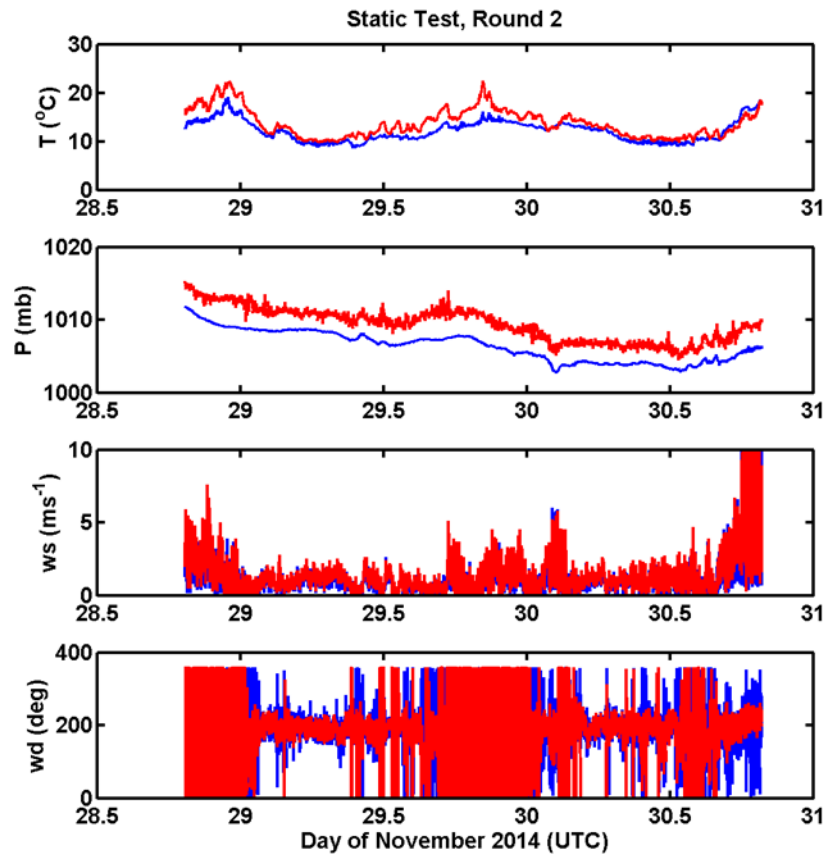


Figure 32. Time variation of Airmar 1 Hz measurements during static testing where blue and red indicates NPS Met and Airmar measurements, respectively.

The Airmar temperature is consistently higher than the NPS Met temperature during the daytime. The largest difference at the mid-day can be as high as 5°C. At night, the Airmar temperature is slightly higher with a much smaller discrepancy compared to the daytime overestimated values (Figure 32). This diurnal variation clearly indicates the effect of solar radiation on the Airmar temperature measurements. This is expected as the Airmar temperature sensor is housed in a ~3 mm diameter void with plastic surroundings. This housing was not designed for optimal natural ventilation as the Rotronic housing.

Figure 33 shows the comparison of the Airmar pressure, temperature, and wind speed with the respective NPS Met measurements. To further study the effect of solar heating on the Airmar temperature, I separated the data into day and night segments. Data

collected between 1400–0100Z are considered daytime data and are plotted in red, while data collected between 0100–1400Z are considered nighttime data and are plotted in blue. The air temperature collected when wind speed was less than 2 ms^{-1} are also circled in green. It is clear from Figure 33b that the majority of the static tests were made in low wind conditions. Furthermore Figure 33b shows that the majority of the overestimated temperature measurements occurred during low wind conditions.

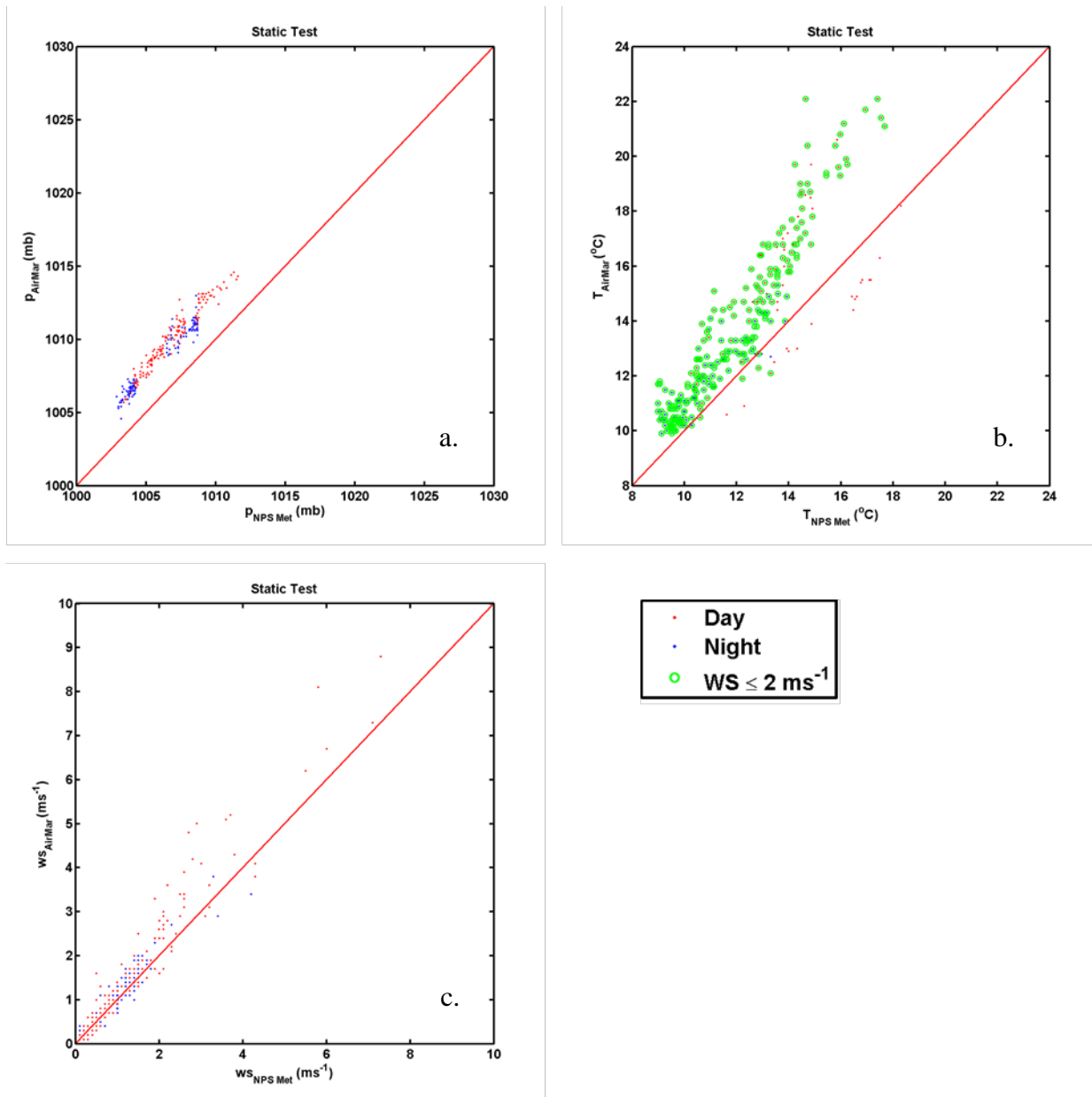


Figure 33. Comparison of 10 minute averaged static Airmar and NPS Met measurements for a) pressure; b) air temperature; c) wind speed.

Table 8 summarizes the statistical comparison between the Airmar and the NPS Met data. Overall, the Airmar follows the mean trends well, but may deviate considerably on specific instances. The Airmar temperature measurements, in particular, appear to suffer from solar heating of the sensor housing particularly in low wind conditions. More testing is needed to better understand the Airmar performance for pressure and quantify the temperature error associated with sensor heating.

Airmar vs NPS Met Static Testing (1Hz Data)					
	Press (mb)	Temp (C)	Daytime Temp (C)	Nighttime Temp (C)	Wind Sp (ms ⁻¹)
Mean Error	2.94	1.58	2.13	1.03	0.17
Error Std Dev	0.58	1.44	1.78	0.62	0.39
Abs Error	2.94	1.76	2.47	1.04	0.26

Table 8. Statistical comparison of Airmar and NPS Met measurements using 10 minute averages of the 1 Hz raw data during November 2014 static testing.

C. EVALUATION OF AIRMAR MEASUREMENTS COLLECTED BY LRI AND NAVO SHARCS

The Airmar PB200, as the default METOC sensor on the LRI METOC Plus SHARCS, has been used in multiple at-sea measurements and demonstrations. Two of these data collection efforts are used here to further evaluate the Airmar data quality using nearby buoys. The LRI PacX SHARC orbited NDBC buoy 46092 in Monterey Bay during November 2011. Two NAVO SHARCS also orbited near this same buoy from September-December 2012. The proximity of SHARCS to the NDBC buoy permits further evaluation of the SHARC Airmar PB200 at-sea performance using the hourly buoy data. This data was interpolated onto the time of the SHARC data for direct comparison. The results are provided below.

1. PacX SHARC Data

LRI launched four SHARCS from San Francisco in November 2011 to begin the PacX event. During the last week of November 2011, three of the four SHARCS remained within 15 km of buoy 46092 for approximately four days. The SHARCS took turns orbiting the buoy and then loitering nearby. The SHARC sensors should be calibrated at its best at the time of this data collection since the SHARCS had only

recently departed San Francisco. Figure 34 shows the LRI PacX SHARC tracks during this timeframe. The inner box shows the tracks that are within 15 km of buoy 46092.

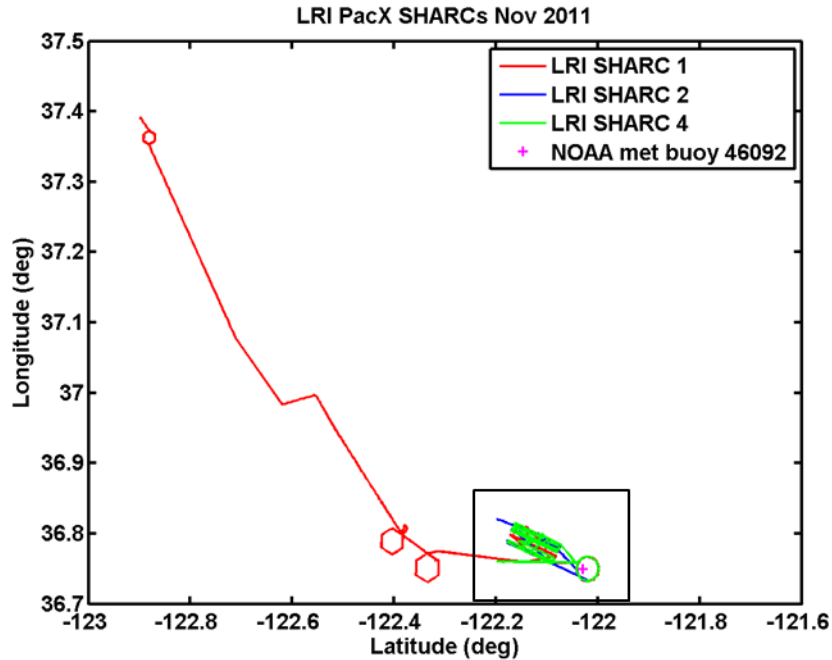


Figure 34. SHARCs 1, 2, and 4 path during November, 2012 PacX. The inner box shows tracks within 15 km of buoy 46092.

Figure 35 is the time series plot of the LRI SHARC 10 minute averaged pressure and the NDBC 46092 hourly averaged pressure. There are minor gaps in both the NDBC buoy data and the SHARC Airmar data. As shown in the NPS Airmar datasets, the PB200 measurements depict the pressure trend well but with outliers that appear unreasonable. Figure 36 shows the scatter plot of the SHARC and buoy pressure data. This figure also reveals that the two measurements are generally correlated but with some “bad” values from the SHARC Airmars.

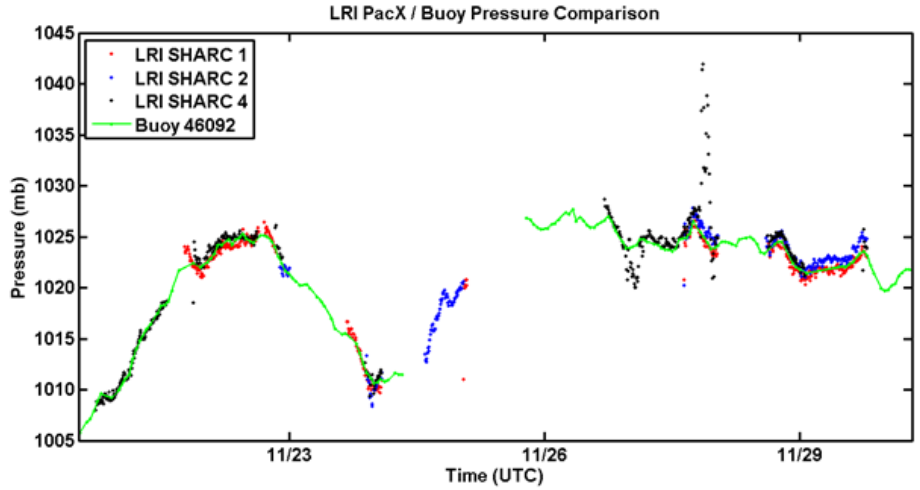


Figure 35. Time variation of the PacX SHARC and buoy 46092 pressure measurements.

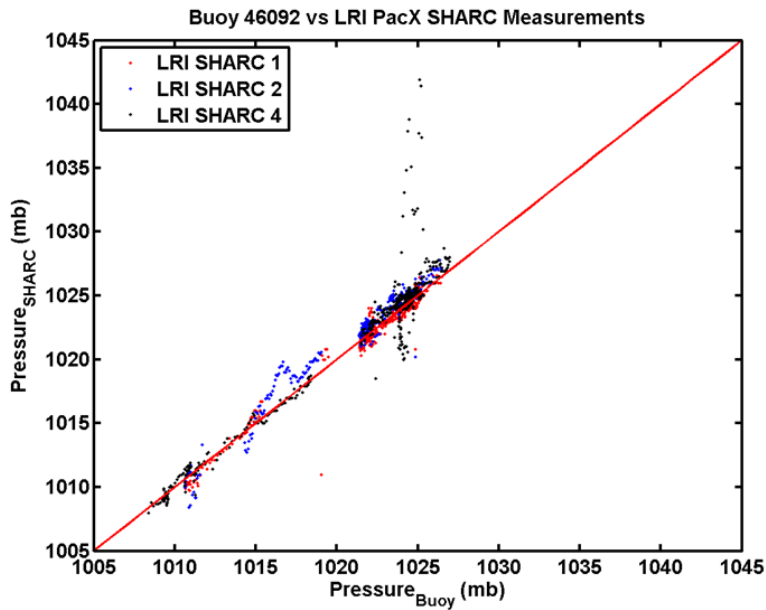


Figure 36. Comparison of the LRI SHARC and NDBC pressure measurements.

Figure 37 shows the time series of the LRI SHARC and NDBC buoy wind speed and wind direction measurements. The buoy measured wind speed appears to undergo a diurnal cycle that the Airmar also shows. The three SHARCs all overestimated wind speed on November 29, 2011. The reason for this systematic departure is not known. The wind direction shifts from Southeast to North during this PacX period that the Airmar

largely detects, as well. The scatter plots (Figure 38) reveal less correlation in these data sets, however, than in the NPS at-sea datasets where the sensors are exactly collocated.

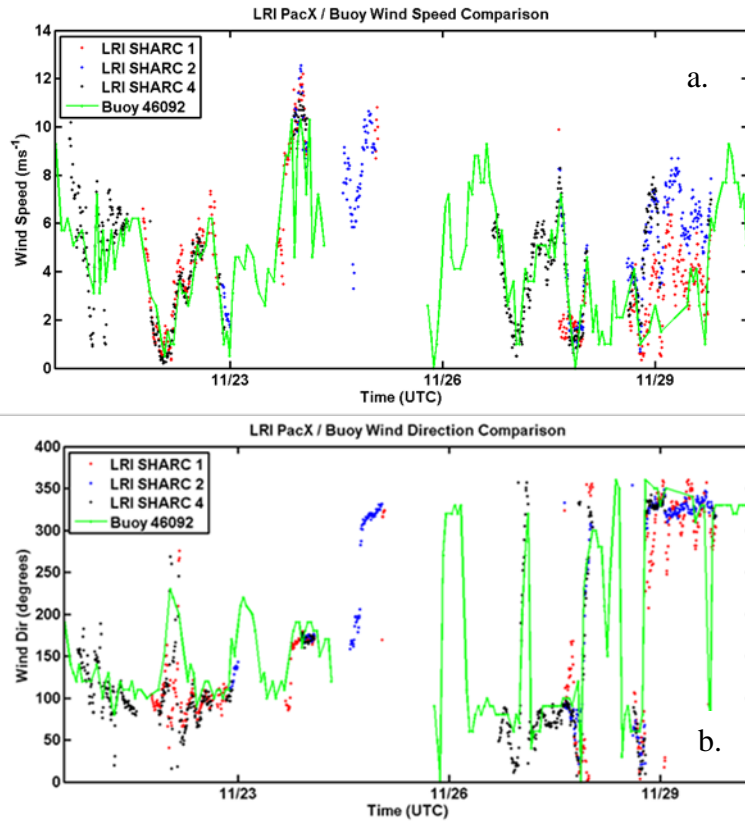


Figure 37. Same as Figure 35, except for a) wind speed; b) wind direction measurements.

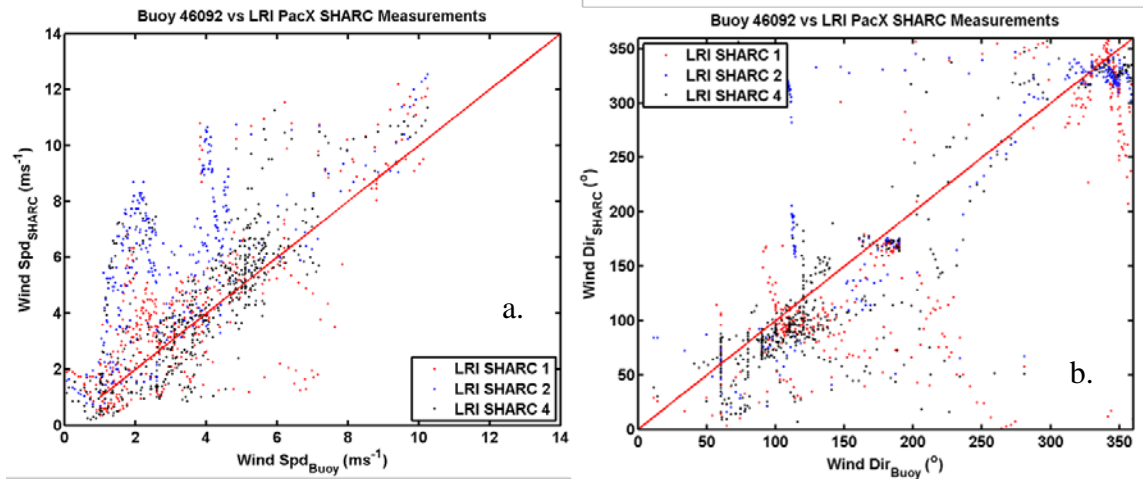


Figure 38. Same as Figure 36, except for a) wind speed measurements; b) wind direction measurements.

The buoy air temperature measurements during this time period vary diurnally (Figure 39). The SHARC data also follow this pattern but appear to overestimate the peak temperatures, and underestimate the lows. This figure also indicates that there may be multiple factors affecting the quality of the Airmar measurement resulting in the sporadic consistency shown in the time series plot. This is reflected in the scatter plot as well with small correlations of the two measurements.

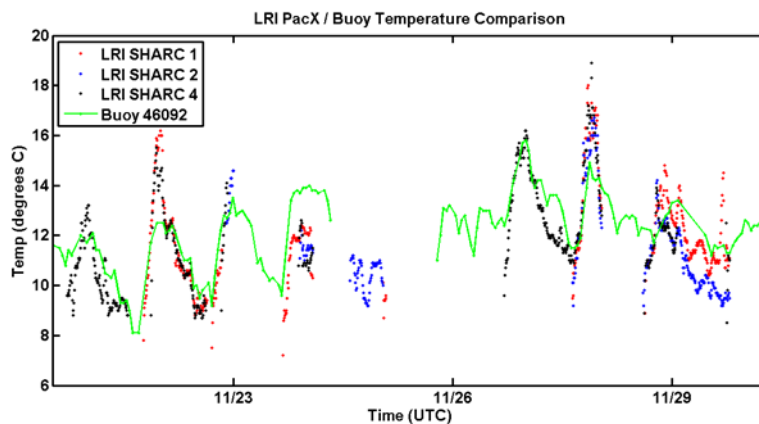


Figure 39. Same as Figure 35, except for air temperature.

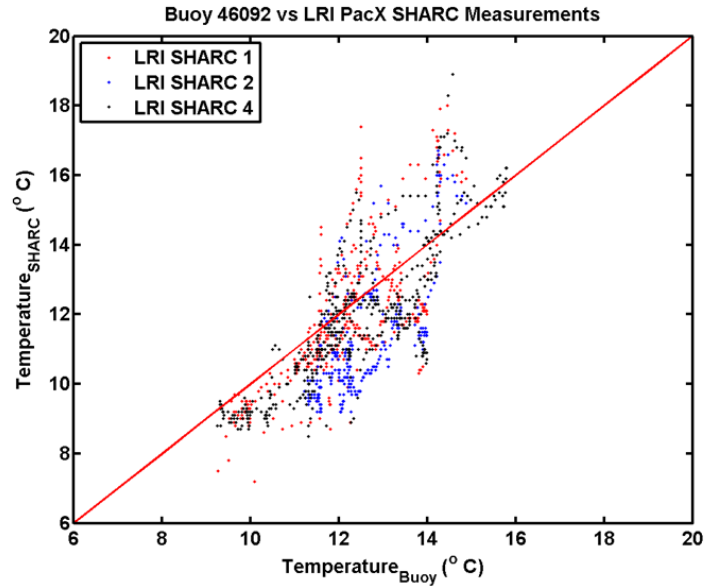


Figure 40. Same as Figure 36, except for air temperature measurements.

To further analyze the SHARC Airmar temperature measurements and examine the effect of solar heating on the resultant data, I separated the data into daytime and nighttime observations following the same method used on the NPS static data. Again, the air temperature that coincided with wind speed less than or equal to 2 ms^{-1} was circled in green. As seen in Figure 41a, the vast majority of the overestimated Airmar temperatures occur during the day. Figure 41b reveals a direct association between overestimated air temperature data, daytime heating, and low wind speed. This plot indicates that the solar heating effect on the Airmar can be significant.

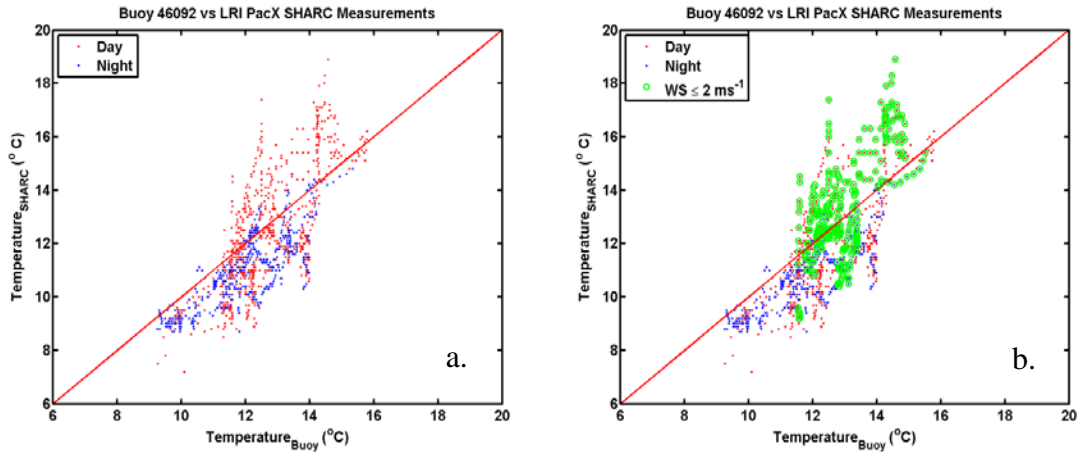


Figure 41. Comparison of the LRI PacX SHARC and NDBC buoy 46092 measured air temperature with a) daytime data in red and nighttime data in blue; b) when wind speed was less than 2 ms^{-1} (circled in green) to examine the effects of solar heating on the Airmar.

2. NAVO SHARC Airmar Data Analysis

From September-December 2012, NAVO steered two of their SHARCs to orbit in Monterey Bay. During this time, the NAVO SHARCs were within 15 km of the NDBC buoy 46092. The NAVO SHARC tracks are shown in Figure 42. NAVO powered down the SHARC Airmar weather stations for long periods of time to conserve power (S. Crossland 2014, NAVO, personal communication) but did collect approximately 12 days of near surface measurements. Figure 43 shows the wind direction from the entire period to illustrate the presence of the Airmar weather data gaps. Of note, the buoy wind direction resolution is 10 degrees while the SHARC Airmar resolution is 1 degree. The scatter plot, Figure 44, reveals large number of correlated measurements from the two systems, although we can see clearly a large number of uncorrelated results as well.

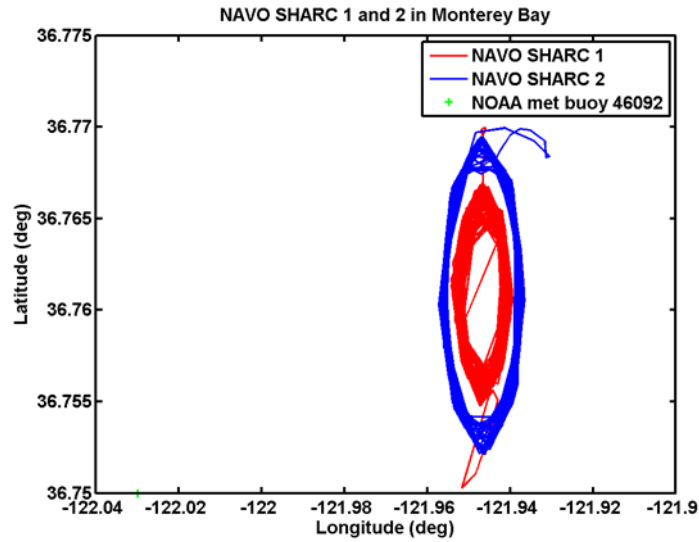


Figure 42. NAVO SHARC tracks within 15 km of buoy 46092 from September – December 2012 in Monterey Bay. Location of Buoy 46092 is shown in green on the horizontal axis.

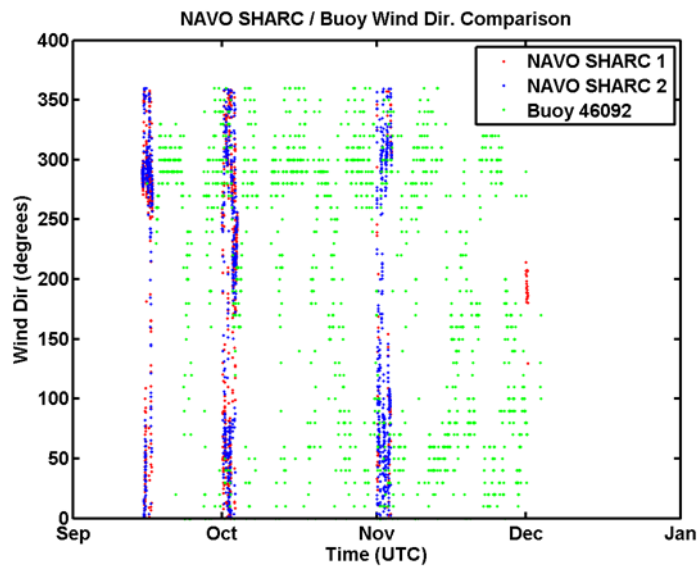


Figure 43. Time variation plot of the NAVO SHARC Airmar and NDBC buoy 46092 wind directions from the entire intercomparison mission between September and December 2012.

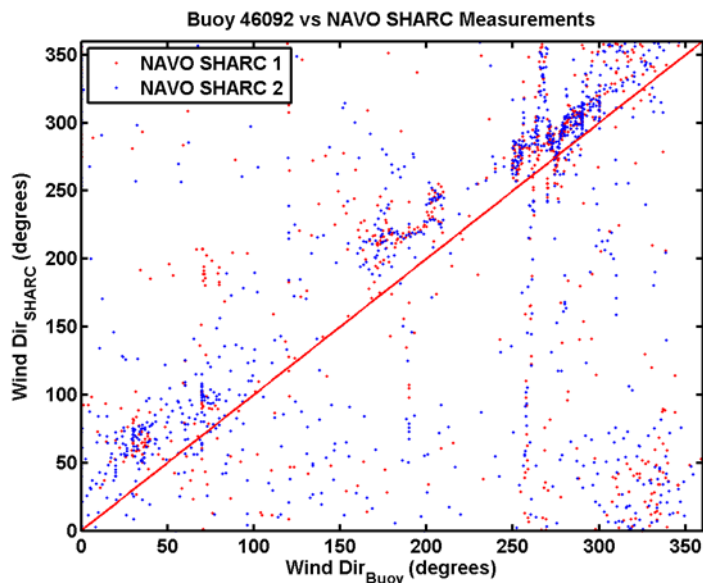


Figure 44. Comparison of the NAVO SHARC and NDBC buoy 46092 wind direction measurements.

For the next set of time series plots, the time periods in October and November 2012 when both the NAVO SHARC and NDBC buoy were collecting data are isolated to show more details (Figure 45). Figures 45a and 45b contain the wind speed data collected by the NAVO SHARCs and NDBC buoy 46092 in October and November, respectively. Figures 45c and 45d show the pressure measurements for these platforms in October and November, respectively. Both the sets of time series plots and the scatter plots shown in Figures 46a and 46b indicate that the SHARC Airmar data have generally good correlation with the NDBC buoy data. There are, however, outliers and the SHARC pressure measurements, in particular, are prone to have outliers. Again, these plots indicate that the Airmar provides good trend information but not the details, and require data quality control.

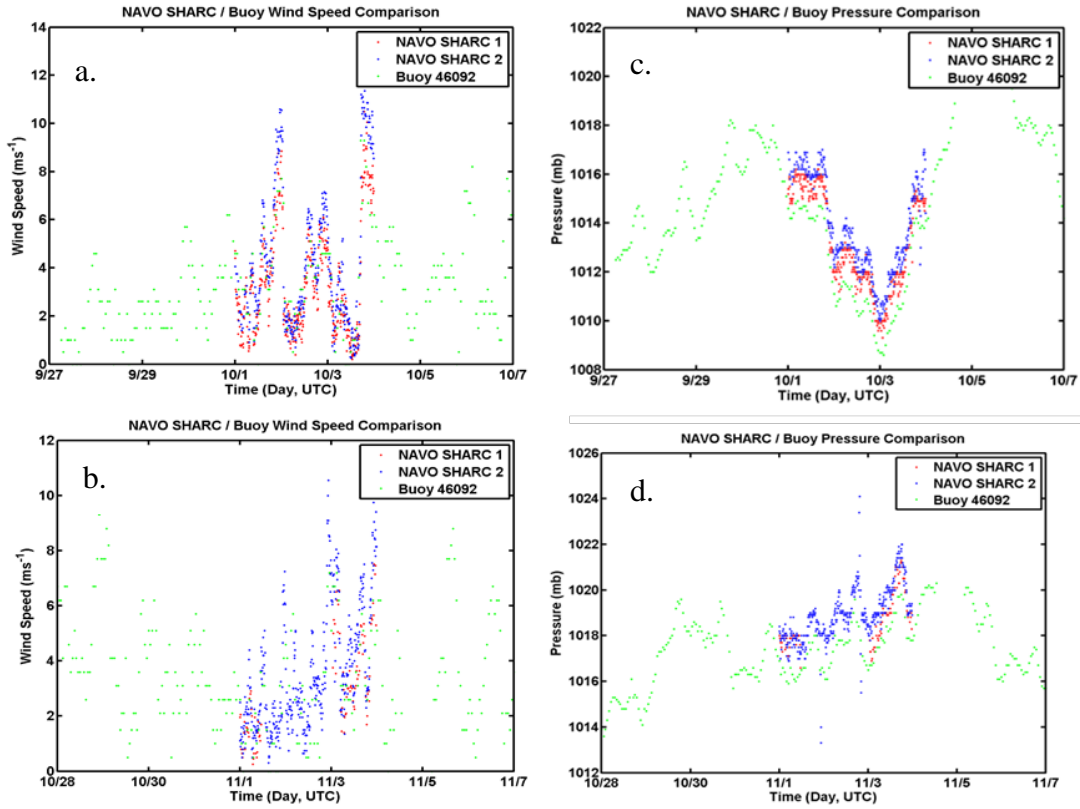


Figure 45. Time variation of the NAVO SHARC and NDBC buoy 46092 measurements with a) wind speed centered around October 1, 2012; b) wind speed centered around November 1, 2012; c) pressure centered around October 1, 2012; d) pressure centered around November 1, 2012.

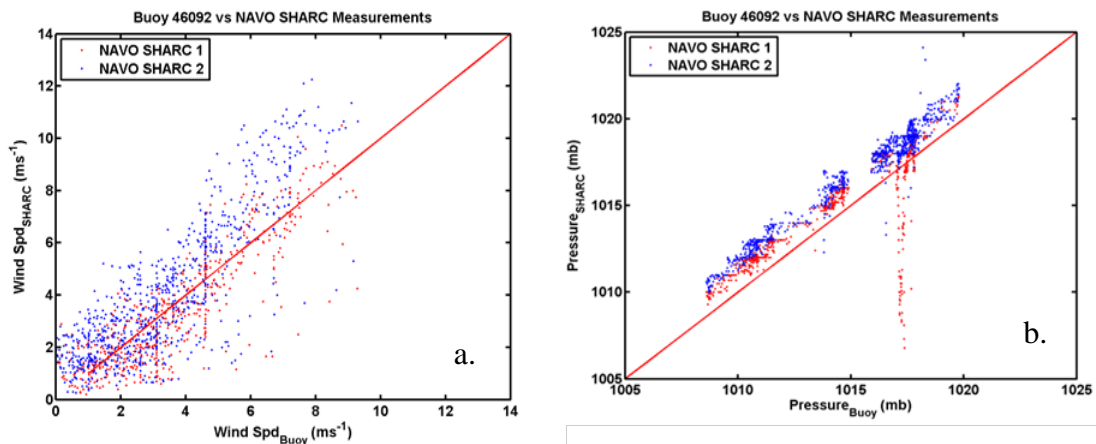


Figure 46. Comparison of the NAVO SHARC and NDBC buoy 46092 a) wind speed measurements; b) pressure measurements.

Figure 47 shows the time series plots of the NAVO SHARC and NDBC buoy 46092 air temperature measurements centered about October 1, 2012 and November 1, 2012, respectively. The NAVO SHARC data follows the general diurnal cycle but, overall, the SHARC overestimates the air temperature. Following the same process used with the LRI PacX data to examine the effect of solar heating on the Airmar, I separated the day and night observations (Figure 48a) and then circled data that corresponded to periods of low wind speed (Figure 48b). While the overly high temperatures are not as well correlated with daytime heating errors, they are strongly associated with low wind speed.

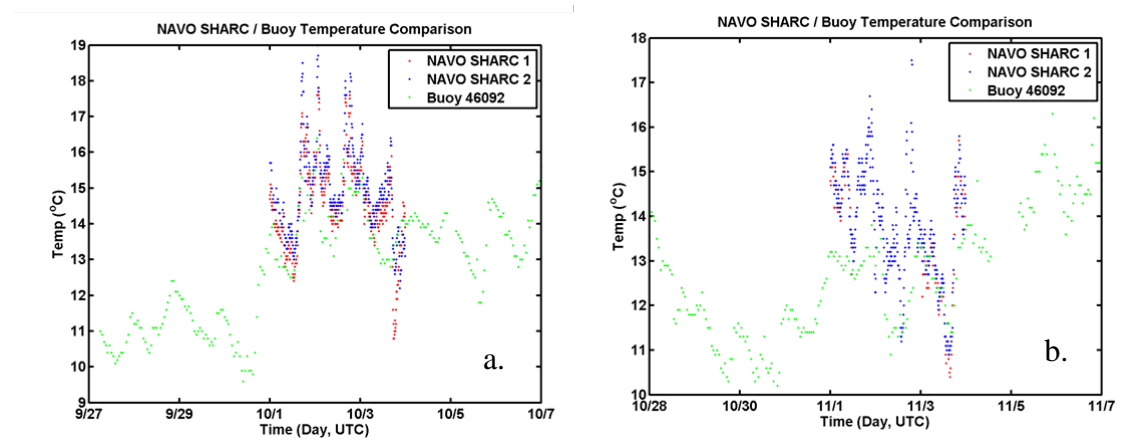


Figure 47. Same as Figure 45, except for air temperature.

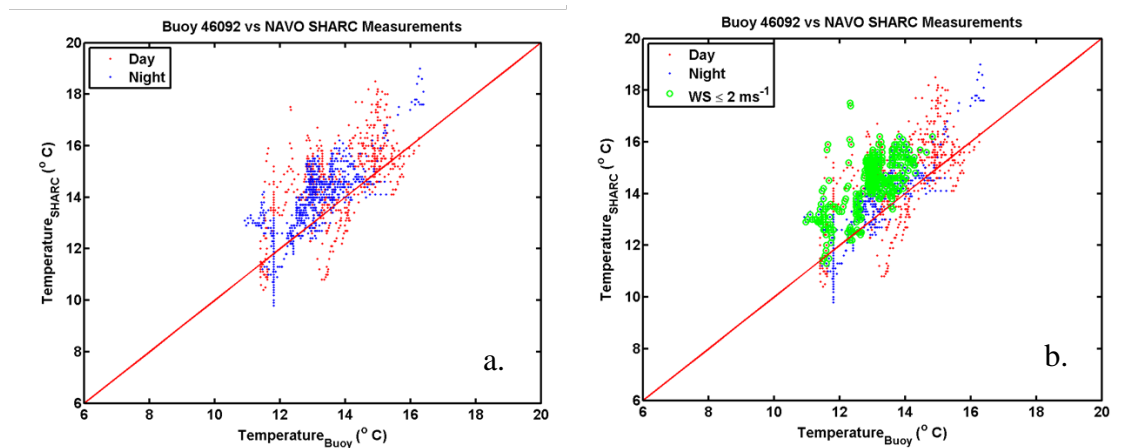


Figure 48. Same as Figure 41, except for the NAVO SHARC.

3. Airmar Data Set Conclusions and Statistics

Overall, the LRI PacX and NAVO Airmar datasets accurately depict longer scale trends. The data requires quality control, however. The Airmar temperature sensors seem to have different bias day and night, suggesting the role of solar heating resulting in the additional errors. Table 9 summarizes the statistical evaluation of Airmar measurements against other known sensor packages. Of note, the LRI and NAVO Airmar have temperature mean errors of 2.02 and 1.00 °C during conditions of daytime heating and low winds. To combat these issues, the Airmar sensor should be calibrated separately for daytime and nighttime. Specifically during the daytime, the Airmar should be calibrated against a high quality, temperature sensor in aspirated radiation shield. Since the Airmar does not have a well-ventilated radiation shield, the magnitude of solar heating effect is greater than that experienced by the NPS Met and NDBC buoy sensors.

Airmar vs NPS Met At Sea (10 Minute Averages)			
	Press (mb)	Temp (C)	Wind Sp (ms ⁻¹)
Mean Error	-0.39	3.28	0.09
Error Std Dev	0.21	1.00	0.19
Abs Error	0.40	3.28	0.18
Corr Coef	0.81	0.64	1.00
NAVO SHARCs vs NDBC Buoy 46092			
	Press (mb)	Wind Sp (ms ⁻¹)	Day Temp with Winds <2 (ms ⁻¹)
Mean Error	1.08	0.36	2.02
Error Std Dev	1.47	1.41	0.88
Abs Error	1.50	1.13	2.03
Corr Coef	0.89	0.82	0.65
	Temp (C)	Daytime Temp (C)	Nighttime Temp (C)
Mean Error	0.75	0.84	0.68
Error Std Dev	1.06	1.20	0.93
Abs Error	1.05	1.16	0.96
Corr Coef	0.75	0.70	0.80
LRI PacX SHARCs vs NDBC Buoy 46092			
	Press (mb)	Wind Sp (ms ⁻¹)	Day Temp with Winds <2 (ms ⁻¹)
Mean Error	0.34	1.07	1.00
Error Std Dev	1.43	2.00	1.31
Abs Error	0.73	1.61	1.31
Corr Coef	0.96	0.68	0.80
	Temp (C)	Daytime Temp (C)	Nighttime Temp (C)
Mean Error	-0.57	-0.32	-0.97
Error Std Dev	1.33	1.51	0.83
Abs Error	1.18	1.27	1.04
Corr Coef	0.73	0.72	0.81

Table 9. Statistical comparison between SHARC/Airmar at-sea environmental measurements and measurements from known, high quality instruments.

THIS PAGE INTENTIONALLY LEFT BLANK

V. EXAMPLE OF SHARC-BASED NEAR SURFACE MEASUREMENT FOR NAVAL APPLICATIONS

In addition to validating the quality of the NPS Met sensors, the suitability of using the NPS Met near surface mean observations for Naval applications is examined here. The NPS Met at-sea measurements were used as inputs to the COARE algorithm to calculate surface fluxes of momentum, sensible, and latent heat, the near surface mean thermodynamic profiles, and the EDH. This step also further evaluates the suitability of the SHARC as a platform for obtaining high quality measurements for input into coupled forecast models and EM propagation prediction models.

A. SURFACE FLUX

THE NPS Met mean air temperature, SST, wind speed, and RH were input into the COARE algorithm to derive parameterized momentum, sensible heat, and latent heat fluxes. These derived fluxes were then compared to the turbulent fluxes measured by the MASFlux buoy. The MASFlux buoy includes a sonic anemometer, mounted at 3.48 m, which directly measures virtual temperature and 3-dimensional wind components at a sampling rate of 20 Hz, which yield virtual sensible heat and momentum fluxes using the eddy correlation (EC) method.

Figure 49 shows the time series plots of NPS Met and MASFlux surface fluxes derived using mean measurements and COARE, and the fluxes from the EC method, for each day of at-sea testing. The derived fluxes from the NPS Met and MASFlux compare well to each other and any differences in flux are due solely to differences in the mean quantities. The derived fluxes show the same generally increasing trend as the EC fluxes on July 29 and July 30, 2014, but do not capture as much variability as the directly measured fluxes (Figures 49a and 49b). On August 8, 2014, the MASFlux 3-D sonic measured momentum fluxes are almost 50 percent higher than the fluxes derived from the NPS Met and MASFlux mean measurements (Figure 49c). This difference is likely due to the high swell conditions encountered that day. The buoy, the SHARC, or both platforms may have been in the wave boundary layers where basic assumptions of MOST

and COARE are violated. If the platforms were within the wave boundary layers, this factor would also negate the assumption of constant fluxes within the surface layer.

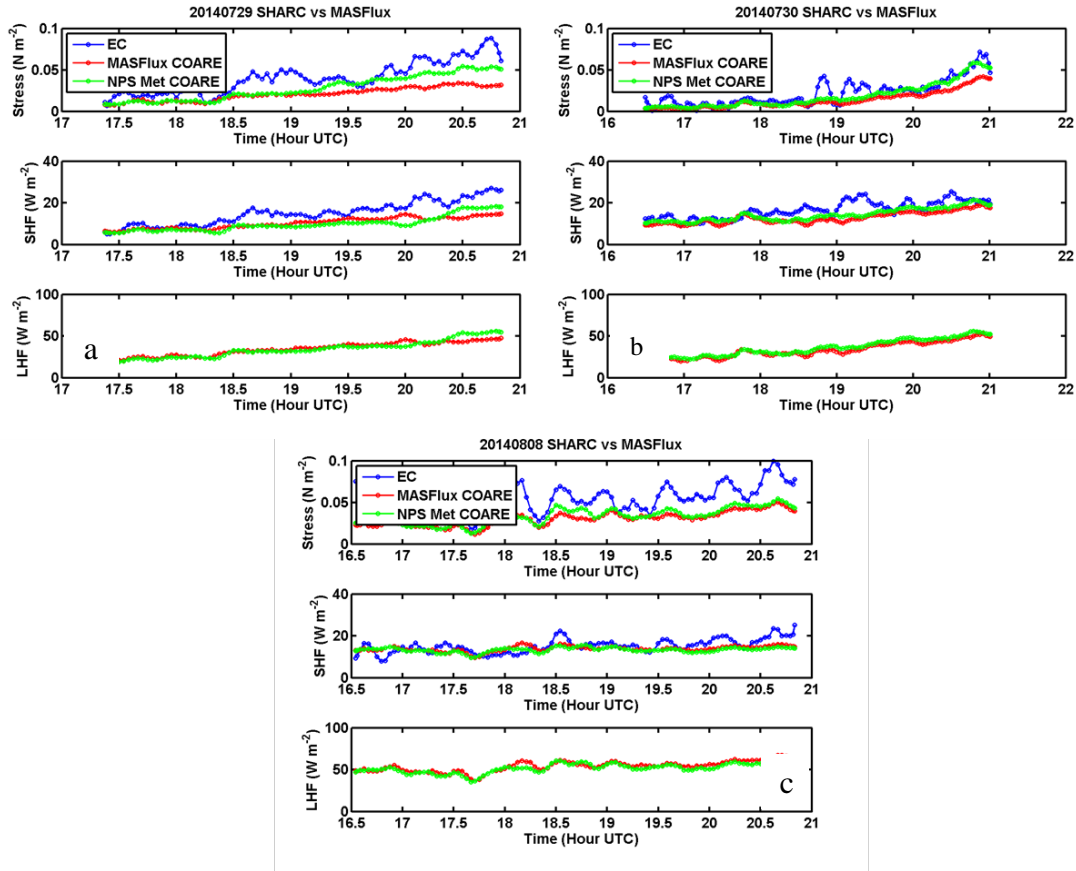


Figure 49. Time variation of NPS Met and MASFlux surface fluxes derived using mean measurements and COARE, and the fluxes from the EC method on a) July 29, 2014; b) July 30, 2014; c) August 8, 2014.

Figures 50 is the scatter plot of NPS Met parameterized momentum flux versus that from the MASFlux using the EC method. Similarly, Figures 51 is the scatter plot of NPS Met parameterized virtual sensible heat flux versus that from the MASFlux using the EC method. Although the mean measurements and COARE tended to underestimate the fluxes, both of these plots show generally good correlation between the derived and measured fluxes on July 29, 2014 and July 30, 2014. The correlation is poor, however, on August 8, 2014. Again, if the SHARC platform was in the wave boundary layers, then

COARE would be insufficient for deriving flux values from mean measurements and hence the poor correlation with EC fluxes shown in Figures 50 and 51.

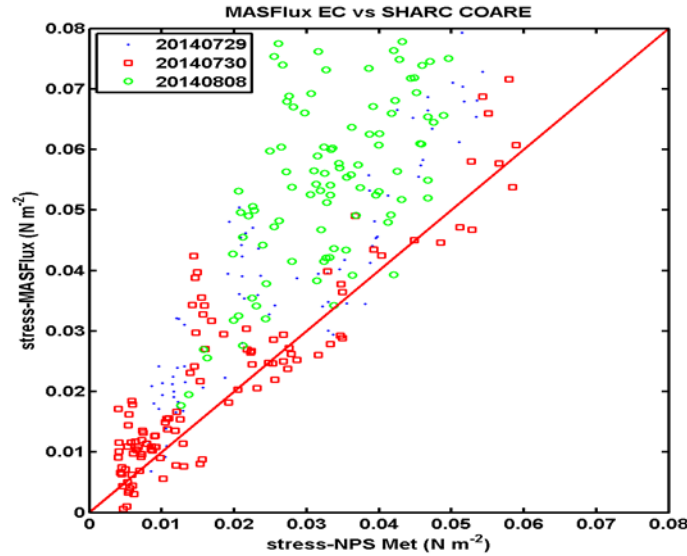


Figure 50. Comparison of NPS Met momentum flux derived using mean measurements and COARE, and the momentum flux from the EC method.

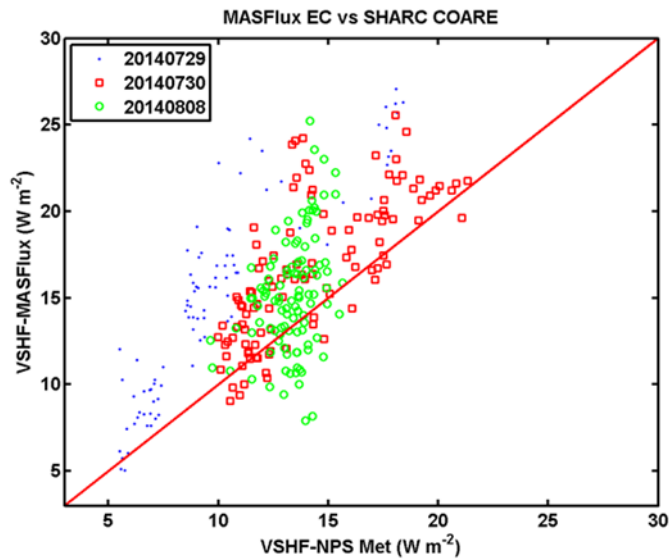


Figure 51. Same as Figure 50, except for virtual sensible heat flux.

B. NEAR SURFACE PROFILES AND EDH CALCULATIONS

In addition to surface fluxes, the SHARC mean measurements and the output of the COARE algorithm can be used to derive the surface layer vertical profiles of mean wind, potential temperature and specific humidity. The thermodynamic profiles can then be used to determine the vertical profile of the refractivity index or the modified refractive index, M (Eq. 9), which determines EM ducting and propagation paths in the surface layer. Figure 52 shows an example of two profiles calculated using the mean measurements collected by the SHARC and NPS Met sensors on August 8, 2014. As described in Chapter II, the EDH is one measure of the property of the evaporative duct and its ability to trap EM waves and is defined by the height at which dM/dz is equal to zero. The evaporation duct strength (EDS) is defined as the M - difference between the EDH level and the surface. Figure 53 shows a plot of the EDH and EDS at 10 minute intervals on August 8, 2014 as determined using SHARC mean measurements and the derived M vertical profile. The red and blue lines indicate the time when the example profiles in Figure 52 are taken and the associated EDH and EDS at these time instances. The SHARC's ability to collect quality near surface measurements allows users to obtain near real time vertical profiles and the associated EDH and EDS quantities which can be input to the atmospheric propagation models, such as AREPS, for prediction of EM propagation as a tactical decision aid.

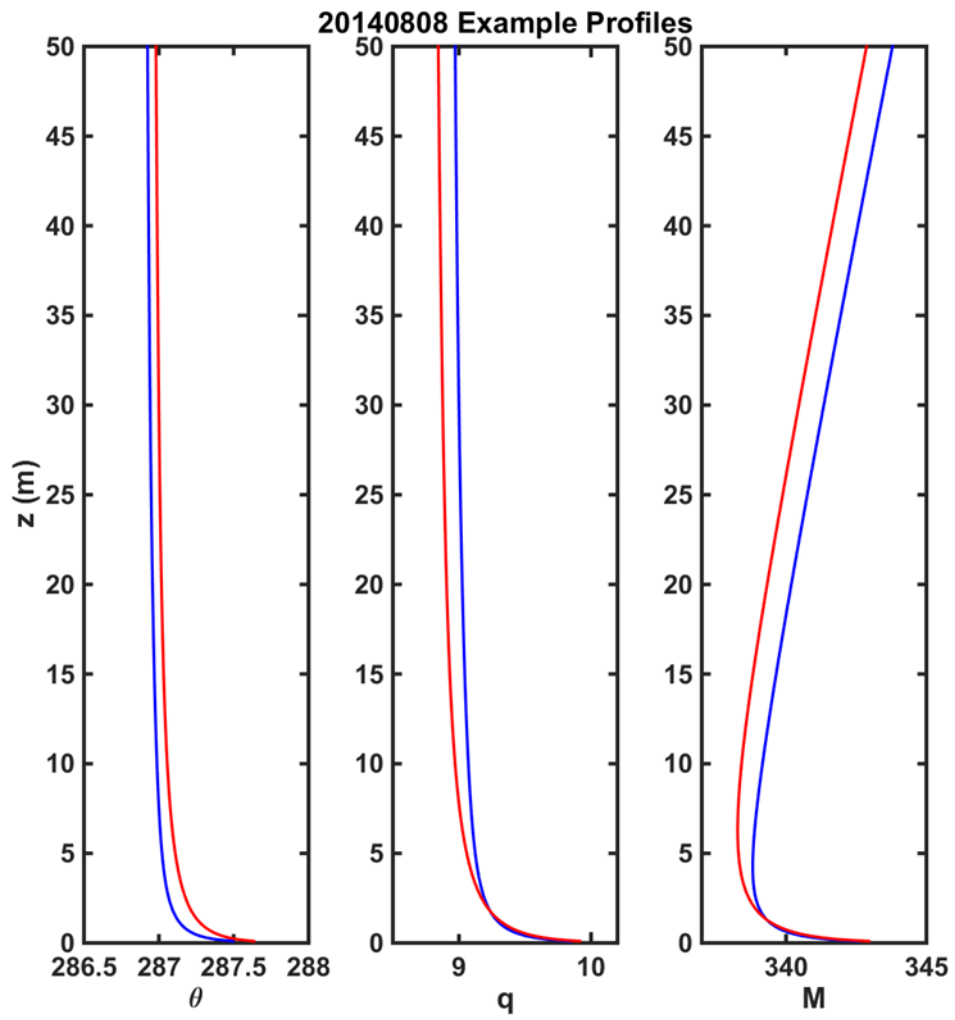


Figure 52. Example vertical profiles derived using SHARC measurements from August 8, 2014 at-sea testing and the output of COARE algorithm.

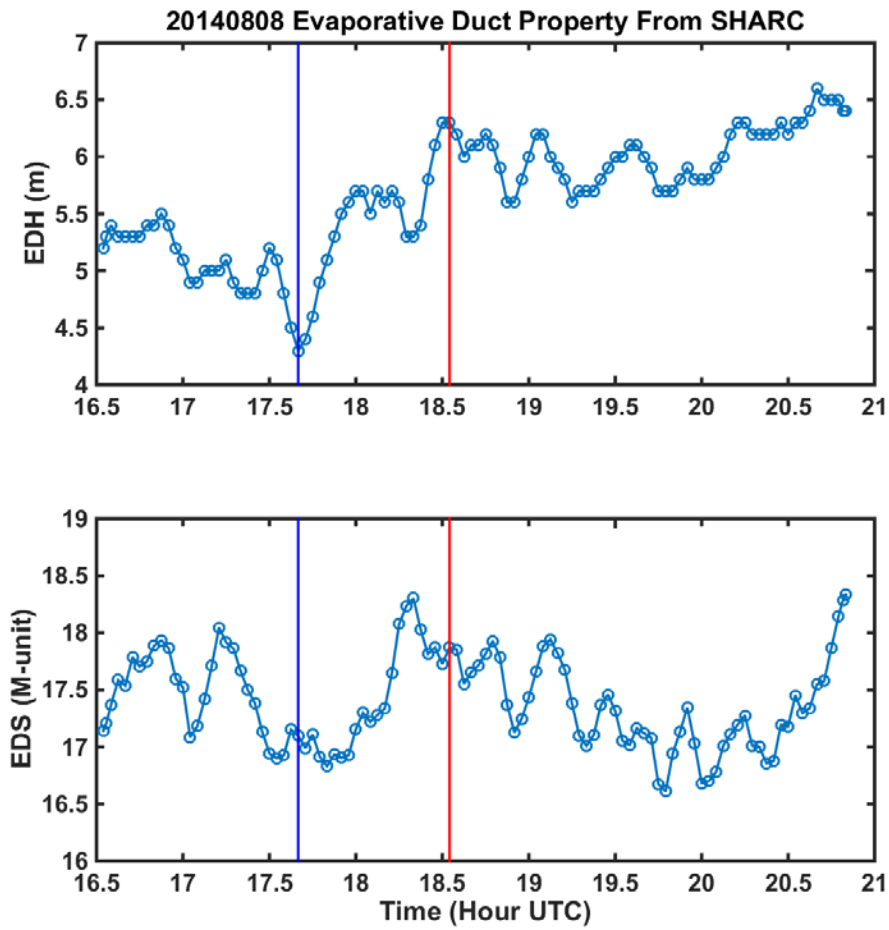


Figure 53. EDH and EDS calculated from the SHARC derived near surface vertical profiles during August 8, 2014 at-sea testing.

VI. CONCLUSIONS AND RECOMMENDATIONS

A. SHARC, NPS MET, AND AIRMAR CONCLUSIONS

The SHARC is a capable, suitable, and advantageous moving platform for collecting near surface measurements. The SHARC platform offers numerous new and exciting capabilities, including its high endurance and ability to withstand harsh conditions. Additionally, operators can steer the SHARC to areas of interest and have it remain on station. Critically, this thesis also shows that the SHARC platform does not distort the mean measurements collected from it.

The NPS Met is proven to be better suited for obtaining high quality mean measurements for air-sea interaction studies and Naval applications than the default Airmar PB200 sensor package. The NPS Met and the known, high quality MASFlux mean measurements are highly correlated and display only small biases due to spatial and temporal variability. The NPS Met package also measures RH and SST which are not available via the Airmar, and are critical to determining surface fluxes, near surface profiles, and properties of the EDH. The low power consumption of the NPS Met also lends itself well to long endurance missions on the SHARC. Although solar radiation heating of the air temperature sensor does affect the NPS Met and all naturally-ventilated systems, the radiation shield minimizes this effect.

The Airmar PB200 captures mean trends adequately but requires individual instrument calibration and data quality control. The Airmar temperature sensor requires careful calibration, both to eliminate biases and to account for solar heating errors. As the Airmar does not have an effective radiation shield, the magnitude of solar heating is greater than that experienced by the NPS Met and NDBC buoy sensors, and the effect is especially evident in low wind conditions. The Airmar pressure measurements appear to be inconsistent at times and also require data quality control. Finally, the Airmar does not sample RH or SST which are required for many Naval applications.

B. RECOMMENDATIONS FOR FUTURE WORK

In order to maximize SHARC and NPS Met usages and functioning, several areas of research require more work. For groups continuing to use the default Airmar weather instrument, there needs to be a more quantitative process or algorithm to provide pressure and temperature data quality control. Additionally, the suitability of the SHARC for measuring waves and sea state should be evaluated. As part of this process, the wave sensor recommended by LRI SHARC's METOC Plus model should be further evaluated. The NPS Met and MASFlux measurements and data sets available from NAVO provide an excellent starting point for this task. For the NPS Met package and SHARC platform, future research should focus on the effect of the wave boundary layer on mean and flux measurements, especially during high swell or wave conditions. Finally, the NPS team is in the process of developing a direct flux measuring payload for the SHARC. This new payload will require testing and evaluation, as well.

LIST OF REFERENCES

- Airmar Technology Corporation, cited 2014: Airmar PB200 Specifications. [Available online at <http://www.airmartechology.com/uploads/brochures/pb200.pdf>]
- Andreas, E., P. O. G. Persson, J. E. Hare, 2008: bulk turbulent air-sea flux algorithm for high-wind, spray conditions. *J. Phys. Oceanogr.*, **38**, 1581–1596.
- Babin, S. M., G. S. Young, and J. A. Carton, 1997: A new model of the oceanic evaporation duct. *J. Appl. Meteor.*, **36**, 193–204.
- Bao, J. W., S. A. Michelson, J. M. Wilczak, 2002: Sensitivity of numerical simulations to parameterizations of roughness for surface heat fluxes at high winds over the sea. *Amer. Meteor. Soc.*, **130**, 1926–1932.
- Brown, J. M., L. O. Amoudry, F. M. Mercier, A. J. Souza, 2013: Intercomparison of the Charnock and COARE bulk wind stress formulations for coastal ocean modelling. [Available online at <http://www.ocean-sci.net/9/721/2013/>]
- Businger, J. A., J. C., Wyngaard, Y. Izumi, and E. F. Bradley, 1971: Flux-profile relationships in the atmospheric surface layer. *J. Atmos. Sci.*, **28**, 181–189.
- Charnock, H., 1955: Wind stress on a water surface. *Quart. J. Roy. Meteor. Soc.*, **81**, 639–640.
- Cheney, D. J., 2011: Measurements of the air-sea interface from an instrumented small buoy. M. S. thesis, Dept. of Meteorology, Naval Postgraduate School, 56 pp.
- Edson, J. B., and C. W. Fairall, 1998: Similarity relationships in the marine atmospheric surface layer for terms in the TKE and scalar variance budgets. *Amer. Meteor. Soc.*, **55**, 2311–2327.
- Edson, J. B., T. Paluszkiwicz, S. Sandgathe, L. Vincet, L. Goodman, T. Curtin, J. Hollister, M. Coulton, 1999, August 25: Coupled marine boundary layers and air-sea interaction initiative: Combining process studies, simulations, and numerical models. [Available online at <http://www.whoi.edu/science/AOPE/dept/r5.pdf>]
- Fairall, C. W., E. F. Bradley, J. S. Godfrey, G. A. Wick, J. B. Edson, and G. S. Young, 1996a: Cool-skin and warm-layer effects on sea surface temperature. *J. Geophys. Res.*, **101**, 1295–1308.
- Fairall, C. W., E. F. Bradley, D. P. Rogers, J. B. Edson, and G. S. Young, 1996b: Bulk parameterization of air-sea fluxes for Tropical Ocean-Global Atmosphere Coupled-Ocean Atmosphere Response Experiment. *J. Geophys. Res.*, **101**, 3747–3767.

- Fairall, C. W., E. F. Bradley, J. E. Hare, A. A. Grachev, and J. B. Edson, 2003: Bulk parameterization of air-sea fluxes: Updates and verification for COARE algorithm. *J. Climate*, **16**, 571–591.
- Foken, T., 2006: 50 years of the Monin-Obukhov similarity theory. *Boundary-Layer Meteorol.*, **119**, 431–447.
- Greenert, J., 2012, June 25. *CHINFO News Clip*.
- Griffith, J., K. VanderLugt, M. Cosad, 2012: Long term autonomous ocean remote sensing utilizing the wave glider. [Available online at <ftp://ftp.wmo.int/Documents/PublicWeb/amp/mmop/documents/dbcp/Dhcp45-Workshop-2012/presentations/DBCP-28-Wrk-06-Griffith-Wave-Gliders-Article.pdf>]
- Hine, R., S. Wilcox, G. Hine, and T. Richardson, 2009: The Wave Glider: A wave-powered autonomous marine vehicle. *OCEANS 2009*, 1–6.
- Kalogiros, J., and Q. Wang, 2011: Aircraft observations of sea-surface turbulent fluxes near the California coast. *Boundary-Layer Meteorol.*, **139**, 283–306.
- Konstazer, G. C., 1996: Sensitivity of AN/SPY-1B propagation to evaporation duct heights. JHU/APL Tech. Rep. F2F-94-U-4-012, 34 pp.
- Kraus, E. B., and J. A. Businger, 1994: *Atmosphere-Ocean Interaction*. Oxford University Press, 384 pp.
- Liu, T., Katsaros, and J. A. Businger, 1979: The Liu, Katsaros, and Businger Bulk Atmospheric Flux Computational Iteration Program in Fortran and Basic. NRL Memorandum Report 5291, AD-A156 736, 16 pp.
- Liquid Robotics Inc., cited 2014a: Liquid robotics SV-2 description and specifications [Available online at <http://liquidr.com/resdown/downloads/spec-sheets.html>]
- Liquid Robotics Inc., cited 2014b: METOC and METOC plus model specifications [Available online at http://liquidr.com/products_services/metoc-wave-glider.html]
- Mathur, M. B., T. L. Black, J. P. Gerrity, and M. Baldwin, 1993: Impact of analysis errors over data sparse eastern Pacific Ocean of the ETA Model's forecasts. NMC Office Note 399, 22 pp.
- Monin, A. S., and A. M. Obukhov, 1954: Basic laws of turbulent mixing in the surface layer of the atmosphere. *Tr. Akad. Nauk SSS Geofiz. Inst.*, **24**, 163–187.
- Paulus, R. A. (1989): Specification for evaporation duct height calculations. Technical Document 1596, 31pp.

- Powers, J. G., and M. T. Stoelinga, 2000: A coupled air-sea mesoscale model: experiments in atmospheric sensitivity to marine roughness. *Amer. Meteor. Soc.*, **128**, 208–228.
- R. M. Young Company, cited 2014: Multi-plate radiation shield influence of ventilation rate and sun angle on internal temperature [Available online at file:///C:/00A_Research_Projects/Reference_papers/YoungShield.pdf]
- Readings, C. J., J. Businger, M. Coantic, A. R. Mahoney, and K. Naito, 1969: Heat, moisture, and momentum fluxes in the boundary layer. *Radio Science*, **4**, 1381–1383.
- Rochholz, T. W., 2012: Wave-powered unmanned surface vehicle as a station-keeping gateway node for undersea distributed networks. M. S. thesis, Dept. of Applied Physics, Naval Postgraduate School, 62 pp.
- Rutgersson, A., A. S. Smedman, and U. Hogstrom, 2001: Use of conventional stability parameters during swell. *J. Geophys. Res.*, **106**, 27, 117–27, 134.
- Tsvang, L.R., B. M. Koprov, S. L. Zubkovskii, A. J. Dyer, B. Hicks, M. Miyake, R. W. Stewart, and J. W. McDonald, 1973: A comparison of turbulence measurements by different instruments; Tsimlyansk Field Experiment 1970. *Boundary-Layer Meteor.*, **3**, 499–521.
- Turton, J. D., and D. A. Bennets, and S. F. G. Farmer, 1988: An introduction to radio ducting. *Meteor. Mag.*, **17**, 245–254.
- Twigg, K. L., 2007: A smart climatology of evaporation duct height and surface RADAR propagation in the Indian Ocean. M. S. thesis, Dept. of Meteorology, Naval Postgraduate School, 135 pp.
- Waliser, D. E., R. A. Weller, and R. D. Cess, 1999: Comparisons between buoy-observed, satellite-derived, and modeled surface shortwave flux over the subtropical North Atlantic during the Subduction Experiment. *J. Geophys. Res.*, **104**, 31,301–31,320.
- Wang, D., and R. Allard, 2012: Validation of the operational performance of NAVO SHARC METOC and wave sensor systems. Naval Research Laboratory, 29 pp.
- White, J., S. Filipowski, 2014: Know the environment, know the enemy, know the target. *Proceeding*, 30–35.
- Woods Hole Oceanographic Institution, cited 2014: Ocean atmosphere exchange description and illustration by Doucette. [Available online at http://www.whoi.edu/ooi_cgsn/page.do?pid=53278&tid=1621&cid=70189&article=43126]

- World Meteorological Organization, cited 2014: Observation components of the Global Observing System. [Available online at <http://www.wmo.int/pages/prog/www/OSY/Gos-components.html>]
- Zhu, P., and J. Furst, 2013: On the parameterization of surface momentum transport via drag coefficient in low-wind conditions. *Geophys. Res. Letters*, **40**, 2824–2828.
- Ziemba, D. A., 2013: Ducting conditions for electromagnetic wave propagation in tropical disturbances from GPS dropsonde data. M. S. thesis, Dept. of Meteorology, Naval Postgraduate School, 57 pp.
- Zuniga, C. A., 2013: Small flux buoy for characterizing marine surface layers. M. S. thesis, Dept. of Meteorology, Naval Postgraduate School, 65 pp.

INITIAL DISTRIBUTION LIST

1. Defense Technical Information Center
Ft. Belvoir, Virginia
2. Dudley Knox Library
Naval Postgraduate School
Monterey, California